

Evidence for microscopic kurtosis in neural tissue revealed by Correlation Tensor MRI

Rafael Neto Henriques¹, Sune N Jespersen^{2,3} and Noam Shemesh^{1*}

¹*Champalimaud Research, Champalimaud Centre for the Unknown, Lisbon, Portugal*

²*Center of Functionally Integrative Neuroscience (CFIN) and MINDLab, Clinical Institute, Aarhus University, Aarhus, Denmark.*

³*Department of Physics and Astronomy, Aarhus University, Aarhus, Denmark*

*Corresponding author:

Dr. Noam Shemesh, Champalimaud Research, Champalimaud Centre for the Unknown, Av.

Brasilia 1400-038, Lisbon, Portugal

E-mail: noam.shemesh@neuro.fchampalimaud.org;

Phone number: +351 210 480 000 ext. #4467

Abstract

Purpose: The impact of microscopic diffusional kurtosis (μK) – arising from restricted diffusion and/or structural disorder – remains a controversial issue in contemporary diffusion MRI (dMRI). Recently, Correlation Tensor Imaging (CTI) was introduced to disentangle the sources contributing to diffusional kurtosis, without relying on a-priori microstructural assumptions. Here, we investigated μK in *in vivo* rat brains and assessed its impact on state-of-the-art methods ignoring μK .

Methods: CTI harnesses double diffusion encoding (DDE) experiments, which were here improved for speed and minimal bias using four different sets of acquisition parameters. The robustness of CTI estimates from the improved protocol is assessed in simulations. The *in vivo* CTI acquisitions were performed in healthy rat brains using a 9.4T pre-clinical scanner equipped with a cryogenic coil, and targeted the estimation of μK , anisotropic kurtosis, and isotropic kurtosis.

Results: The improved CTI acquisition scheme substantially reduces scan time and importantly, also minimizes higher-order-term biases, thus enabling robust μK estimation, alongside K_{aniso} and K_{iso} metrics. Our CTI experiments revealed positive μK both in white and grey matter of the rat brain *in vivo*; μK is the dominant kurtosis source in healthy grey matter tissue. The non-negligible μK substantially biases prior state-of-the-art analyses of K_{iso} and K_{aniso} .

Conclusion: Correlation Tensor MRI offers a more accurate and robust characterization of kurtosis sources than its predecessors. μK is non-negligible *in vivo* in healthy white and grey matter tissues and could be an important biomarker for future studies. Our findings thus have both theoretical and practical implications for future experiments.

Index

1. Introduction.....	4
2. Theory.....	7
2.1. Total kurtosis estimates from single diffusion encoding	7
2.2. Correlation Tensor Imaging kurtosis source estimation	8
2.3. Accelerating Correlation Tensor Imaging and increasing its robustness towards higher order effects	9
2.4. Specificity of the improved protocol to different kurtosis sources.....	10
2.4. Diffusion tensor variance approach	11
3. Methods.....	13
3.1 Simulations	13
3.2. MRI experiments	16
4. Results.....	18
4.1. Simulations	18
4.2. MRI experiments	22
5. Discussion.....	29
5.1. Limitations and future work.....	31
6. Conclusion	33
Acknowledgments.....	34
References.....	35
Supporting Information.....	48
Section A – Simulation details (Methods).....	48
Section B – CTI in spherical compartments	50
Section C – Considerations for the “old” CTI approach.....	53
Section D - Precision of Microscopic Kurtosis estimates.....	56
Section E – Auxiliary T2-weighted experiments (Methods)	59
Section F – Long mixing time regime	60
Section G – Data processing (Methods)	62
Section H – MGC kurtosis estimates using sets #2-3	63

1. Introduction

Diffusion MRI (dMRI) has become one of the most important methods for non-invasively probing microstructural features in health and in disease (1–3). Single diffusion encoding (SDE) experiments (4,5) (Fig. 1A) probing diffusion along a single axis, have been widely used to measure the directional apparent diffusion coefficient (6–8), the diffusion propagator from q-space experiments (9–12), the diffusion tensor (13–15) and its time-dependence (16–18), and the diffusional kurtosis (via Diffusional Kurtosis Imaging, (DKI), (19)). Together with microstructural and biophysical models (20–24), SDE has provided important insight into microstructural tissue.

DKI in particular provides important quantitative information on the degree of non-Gaussian diffusion reflected in the diffusional excess-kurtosis (19). DKI has been shown to be very sensitive to, inter-alia, age-related microstructural changes (25–29), ischemia (30,31), tumors (32–34), traumatic brain injury (35,36), and Parkinson’s and Alzheimer’s diseases (37,38). However, the biological interpretation of its measures remains limited because non-Gaussian diffusion may arise from different sources (39–41). Several compartment models have been proposed to relate non-Gaussian diffusion with their biological underpinnings (19,42–45); however, the specificity of these models can be severely compromised by their strong assumptions and constraints (46–50).

Unique information about the non-Gaussian nature of tissue diffusion can be resolved using multidimensional diffusion encoding (MDE) strategies (51–53). In contrast to SDE methods, MDE probes diffusion correlations across different dimensions by either including additional pairs of pulse gradients (54–62) or using continuous gradient waveforms with 3D trajectories (63–69). Under the strict Multiple Gaussian Components (MGC) assumption (no time-dependence and no kurtosis arising from restricted diffusion or structural disorder),

Westin et al. showed that MDE can be generally described by tensor-valued encoding information (70). Using different b-tensor shapes, MDE can resolve anisotropic and isotropic kurtosis sources (K_{aniso} and K_{iso}), thereby reporting on the shape and size variances of components represented by diffusion tensors (39,68,71,72). Such MGC analyses are, however, doubly prone to bias arising from restricted diffusion (e.g., upon interaction with microscopic boundaries). First, the MGC analyses of MDE data biases K_{aniso} and K_{iso} when continuous gradient waveforms are long compared to the time it takes to probe the boundaries (67,73,74). Secondly, as we will show in this work, even for fixed diffusion times and tuned MDE, MGC analysis can be biased by non-Gaussian effects (i.e. microscopic kurtosis μK) that arises from restricted diffusion or systems presenting complex microstructural features with characteristic lengths in the order of the probed scales (40,41,49,67,73), e.g. intra-cellular cross-sectional size variance, extra-cellular tortuosity.

Double diffusion encoding (DDE, (5,54–62)) is an MDE variant probing diffusion via two pairs of diffusion pulsed gradients (Fig. 1B). Although previously used without MGC analyses to resolve microscopic anisotropy (61,75–78), recent MGC approaches harnessed DDE's inherent capability to provide both linear and planar encodings, thereby providing sufficient information to resolve K_{aniso} and K_{iso} based on MGC analyses. Moreover, DDE at the long mixing time regime can be used to minimize diffusion time-dependent effects (54,55,57,76,79,80). Although prior DDE studies have attempted to measure μK , orientation dispersion was inherently conflated in the method (41,81). Going beyond the MGC framework, the Correlation Tensor Imaging (CTI) approach (40) was recently introduced for μK measurements. The CTI framework allows the simultaneous decoupling of K_{aniso} , K_{iso} from μK effects without resorting to the multi-Gaussian assumption (40) or without conflation with other mesoscopic effects (41). However, the initial CTI approach (40) can suffer from higher-

order effects, and was quite time-consuming to acquire, thereby limiting its *in vivo* applicability (40).

Here, we aimed to investigate the existence of μK in *in vivo* neural tissues and their impact on the increasingly popular MGC approaches. We first develop an improved and highly accelerated CTI acquisition scheme, which is more robust towards μK estimation, with minimized high-order-term biases. We then investigate the existence of μK in *in vivo* rat brains and investigate its impact on the highly popular MGC approach. Our results provide a new window for quantifying microstructure in health and disease, and show that μK must be considered in future dMRI studies.

2. Theory

2.1. Total kurtosis estimates from single diffusion encoding

The SDE signal attenuation (E_{SDE}) can be expressed (with Einstein summation convention) as the following 2nd order cumulant expansion (19):

$$\log(E_{SDE}(b, \mathbf{n})) = -n_i n_j b D_{ij} + \frac{1}{6} n_i n_j n_k n_l b^2 \bar{D}^2 W_{ijkl} + O(b^3) \quad (1)$$

where b is the b-value defined by $b = (\gamma \delta g)^2 (\Delta - \delta/3)$, \mathbf{n} is the diffusion gradient direction, D_{ij} and W_{ijkl} are the diffusion and excess-kurtosis tensors, and \bar{D} is the mean diffusivity.

To quantify non-Gaussian diffusion decoupled from confounding effects of tissue dispersion, it is also useful to consider the cumulant expansion of powder-averaged SDE signal decays (i.e. signals averaged across multiple gradient directions) (29,48,76):

$$\log(\bar{E}_{SDE}(b)) = -b D_T + \frac{1}{6} b^2 D_T^2 K_T + O(b^3) \quad (2)$$

where \bar{E}_{SDE} is the powder-averaged SDE signal decay, D_T and K_T are the isotropic diffusivity ($D_T = \bar{D}$) and isotropic excess-kurtosis of powder-averaged signals ($K_T = W_{ijjj}/5 + 2D_{ij}D_{ij}/5\bar{D}^2 - 6/5$) (40). In the absence of exchange, the total kurtosis K_T can be described by the sum of three different sources (40):

$$K_T = K_{aniso} + K_{iso} + \mu K \quad (3)$$

where K_{aniso} is related to tissue microscopic anisotropy μA ($K_{aniso} = 2 \frac{\mu A^2}{D^2}$) (39,65,76,77), and K_{iso} is related to the variance of tissue components' apparent mean diffusivities D_i ($K_{iso} = 3 \frac{V(D_i)}{D^2}$, with $V(D_i)$ representing the variance across the mean diffusivities of tissue components) (39,51). Microscopic kurtosis μK , which was previously referred to as intra-compartmental kurtosis (40), is a weighted sum of different microscopic sources of non-Gaussian diffusion μK_i

$$\mu K = \frac{\langle D_i^2 \mu K_i \rangle}{D^2}, \quad (4)$$

with $\langle \cdot \rangle$ representing the average over tissue components). Here μK_i can be related to non-Gaussian diffusion arising from restricted diffusion (41,82,83) or tissue disorder due to the presence of microscopic hindrances to water molecules, e.g. membranes, organelles, axonal caliber variations etc. (49,84–87). Although the total kurtosis K_T can be estimated by fitting Eq. 2 to data acquired with at least two non-zero b-values, it is important to note that the kurtosis sources in Eq. 3 cannot be decoupled from SDE experiments in a model free manner.

2.2. Correlation Tensor Imaging kurtosis source estimation

Recently, the Correlation Tensor Imaging (CTI) methodology was proposed to resolve different kurtosis sources from DDE signals (40). Fig. 1B shows an illustration of the DDE sequence which probes diffusion using two pairs of pulsed gradients with magnitudes g_1 and g_2 , widths δ_1 and δ_2 , separations time Δ_1 and Δ_2 , and mixing time τ_m (Fig. 1B). Note that the DDE pairs can also be applied along different directions, \mathbf{n}_1 and \mathbf{n}_2 . To probe kurtosis for fixed timing parameters, CTI uses $\delta_1 = \delta_2 = \delta$ and $\Delta_1 = \Delta_2 = \Delta$. Moreover, to avoid diffusion time-dependent biases, CTI is applied to DDE data acquired at long mixing time. In this regime and up to 2nd order in b , the DDE signal attenuation (E_{DDE}) can be expressed as (40,60,76,80):

$$\begin{aligned} \log(E_{DDE}(b_1, b_2, \mathbf{n}_1, \mathbf{n}_2)) &= -(n_{1i}n_{1j}b_1 + n_{2i}n_{2j}b_2)D_{ij} \\ &+ \frac{1}{6}(n_{1i}n_{1j}n_{1k}n_{1l}b_1^2 + n_{2i}n_{2j}n_{2k}n_{2l}b_2^2)\bar{D}^2W_{ijkl} + \frac{1}{4(\Delta - \frac{\delta}{3})^2}n_{1i}n_{1j}n_{2k}n_{2l}b_1b_2Z_{ijkl} + O(b^3) \end{aligned} \quad (5)$$

where $b_1 = (\gamma\delta g_1)^2(\Delta - \delta/3)$ and $b_2 = (\gamma\delta g_2)^2(\Delta - \delta/3)$ are the b-values associated with the two DDE gradients, and Z_{ijkl} is a tensor that approaches the covariance tensor ($Z_{ijkl} \rightarrow 4C_{ijkl}(\Delta - \frac{\delta}{3})^2$) at long mixing times. We previously showed that K_{aniso} , K_{iso} , and μK can in theory be extracted from the tensors of Eq. 5 (40). However, our preliminary validation showed

that high-order-terms $O(b^3)$ can introduce biases on the different kurtosis estimates that depend on dispersion levels. To suppress this dependence, powder-averaged DDE signals (\bar{E}_{DDE}) are used:

$$\begin{aligned}
\log(\bar{E}_{DDE}(b_1, b_2, \theta)) &= -(b_1 + b_2)\bar{D} + \frac{1}{6}(b_1^2 + b_2^2)D^2K_T + \frac{1}{2}b_1b_2\cos^2\theta\bar{D}^2K_{aniso} \\
&+ \frac{1}{6}b_1b_2\bar{D}^2(2K_{iso} - K_{aniso}) + O(b^3)
\end{aligned} \tag{6}$$

where θ is defined as the angle between the gradient directions \mathbf{n}_1 and \mathbf{n}_2 . Note that several different pairs of \mathbf{n}_1 and \mathbf{n}_2 with constant θ evenly sampling a 3D unit sphere are required for powder-averaging (48,76,77) – specific pairs of gradient directions used on this study are shown below. From the parameters of Eq. 6, microscopic kurtosis can be estimated by $\mu K = K_T - K_{aniso} - K_{iso}$ (cf. Eq. 3).

2.3. Accelerating Correlation Tensor Imaging and increasing its robustness towards higher order effects

To accelerate the CTI acquisition, we note that only the four different sets of DDE experiments illustrated in Fig. 1C (in addition to acquisitions without diffusion sensitization, i.e. $b_1 = b_2 = 0$), are required to extract CTI's metrics. The 4 sets are as follows:

1) Powder-averaged signals with $b_1 = b_a$ and $b_2 = 0$. Note that these experiments are equivalent to SDE experiments (Fig. 1C1);

2) Powder-averaged symmetric DDE with diffusion weighting $b_1 = b_2 = b_a/2$ and parallel gradient directions ($\theta = 0^\circ$, Fig. 1C2).

3) Powder-averaged symmetric DDE with diffusion weighting $b_1 = b_2 = b_a/2$ and perpendicular gradient directions ($\theta = 90^\circ$, Fig. 1C3);

4) Powder-averaged symmetric and parallel DDE as 3) but with a different total b-value $b_t = b_1 + b_2 = b_b < b_a$ (Fig. 1C4). Note that all previous sets (1-3) have the same total b-value $b_t = b_1 + b_2$ equal to b_a .

To ensure homoscedastic \bar{E}_{DDE} signals, all four experiment sets should be acquired with a similar number of gradient direction pairs for powder-averaging.

2.4. Specificity of the improved protocol to different kurtosis sources

The analysis to resolve different kurtosis sources proceeds as follows:

a) μK can be extracted from the log difference of powder-averaged signals from the experiments' set #1 and #2:

$$\log(\bar{E}_{DDE}(b_a, 0, 0^\circ)) - \log\left(\bar{E}_{DDE}\left(\frac{b_a}{2}, \frac{b_a}{2}, 0^\circ\right)\right) = \frac{1}{12} b_a^2 D^2 \mu K \quad (7)$$

b) as pointed in previous studies (e.g., (76,77,79)), K_{aniso} can be extracted from the log difference of powder-averaged signal from sets #2 and #3:

$$\log\left(\bar{E}_{DDE}\left(\frac{b_a}{2}, \frac{b_a}{2}, 0^\circ\right)\right) - \log\left(\bar{E}_{DDE}\left(\frac{b_a}{2}, \frac{b_a}{2}, 90^\circ\right)\right) = \frac{1}{2} b_a^2 D^2 K_{aniso} \quad (8)$$

c) to decouple \bar{D} , K_T , and K_{iso} , powder-averaged signals also require at least two non-zero total b-values b_t . Therefore, DDE experiments with symmetric intensities and parallel directions for a lower total b-value $b_t = b_a$ are acquired (set #4).

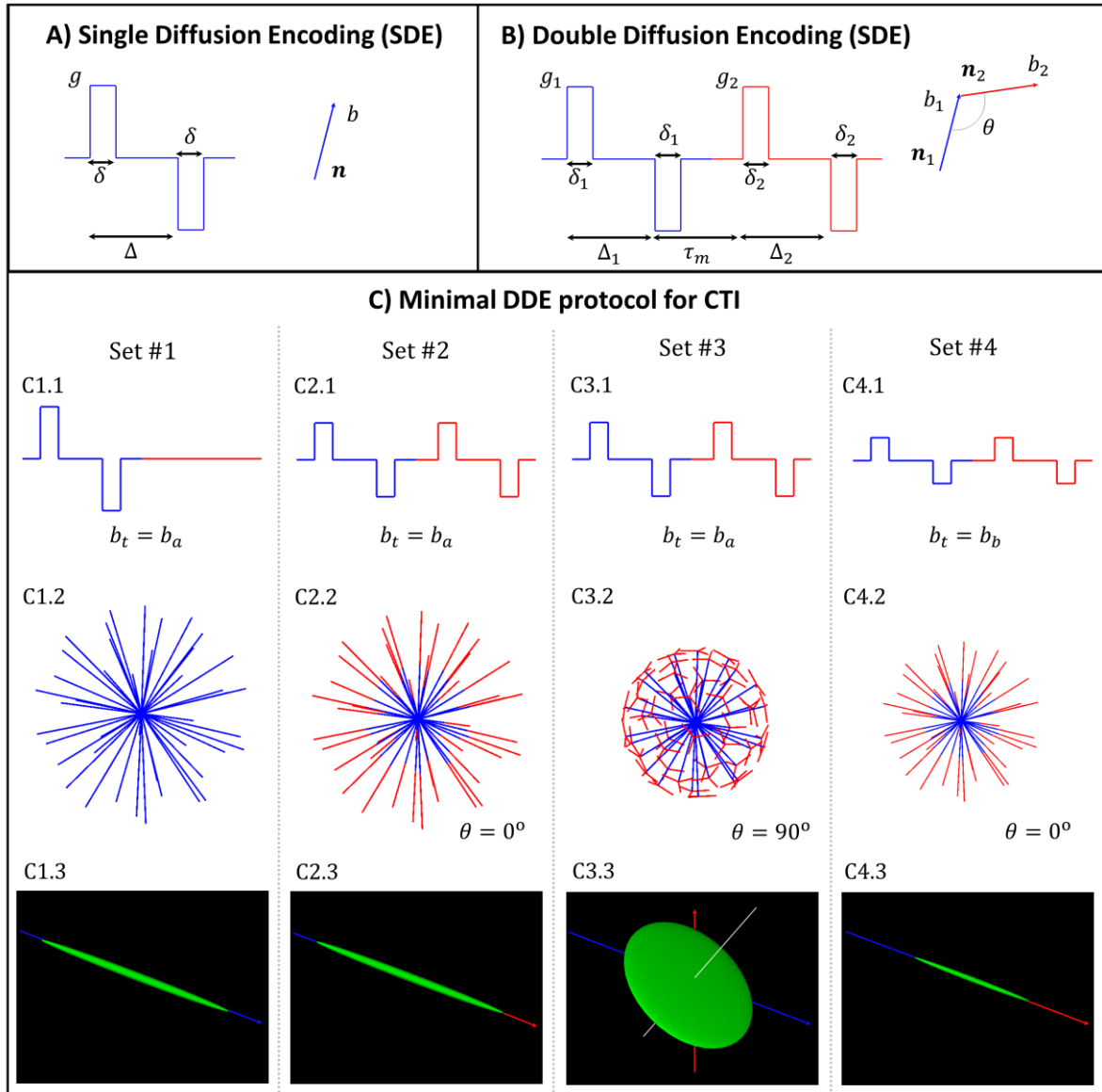


Figure 1 – Experiments for kurtosis source estimation. **A)** Parameters of a standard SDE pulse sequence, where Δ is the diffusion time, δ is the gradient pulse duration, and g is the gradient pulse direction (this sequence can also be described by a gradient direction \mathbf{n} and b-value $b = (\gamma g \delta)^2 (\Delta - \delta/3)$); **B)** Parameters of a standard DDE pulse sequence, where Δ_1 and Δ_2 are the diffusion encoding blocks' diffusion times, δ_1 and δ_2 are their gradient pulse durations, g_1 and g_2 are their gradient intensities and τ_m is the mixing time (i.e. the time between the two diffusion encoding blocks). At the long mixing time, DDE experiments for powder-averaged systems can be fully described by two b-values ($b_1 = (\gamma g_1 \delta_1)^2 (\Delta_1 - \delta_1/3)$ and $b_2 = (\gamma g_2 \delta_2)^2 (\Delta_2 - \delta_2/3)$) and the angle θ between the directions of the two diffusion encoding modules \mathbf{n}_1 (blue) and \mathbf{n}_2 (red); **C)** Parameters for the different data sets required to estimate different kurtosis sources. The diffusion encoding profiles for all data sets are shown in panels C1.1, C2.1, C3.1, and C4.1. The gradient directions used for signal powder-average calculation are shown in panels C1.2, C2.2, C3.2, and C4.2. The equivalent b-tensor shapes for each experiment are shown in panels C1.3, C2.3, C3.3, C4.3.

2.4. Diffusion tensor variance approach

Under the MGC assumption, previous studies showed that K_{aniso} and K_{iso} can be estimated from signals measured using any MDE sequence that probes different b-tensor magnitudes b_t

and shapes. For the sake of simplicity, here we only consider axial tensor-valued experiments (39,51,72), where the b-tensor shape is characterized by a single parameter $b_\Delta \in [-\frac{1}{2}, 1]$.

Thus, the powder-averaged signal is

$$\log(\bar{E}_{MGC}(b, b_\Delta)) = -b_t \bar{D} + \frac{1}{6} b_t^2 \bar{D}^2 K_{iso}^{MGC} + \frac{1}{6} b_t^2 b_\Delta^2 \bar{D}^2 K_{aniso}^{MGC} + O(b^3) \quad (9)$$

Note that K_{aniso}^{MGC} and K_{iso}^{MGC} can be estimated from Eq. 8, using the same dMRI experiments as for CTI, since these correspond to data acquired with at least two b-tensor shapes ($b_\Delta = 1$ for sets #1, #2, and #4, and $b_\Delta = -1/2$ for set #3) and two non-zero b-tensor magnitudes ($b_t = b_a$ for sets #1-3, $b_t = b_b$ for set #4).

3. Methods

3.1 Simulations

The robustness of the different kurtosis source estimation strategies (MGC and CTI) was first assessed via simulations. The full details of the simulations can be found in the Supporting Information, section A. Briefly, synthetic signals were generated for different models with known ground truth kurtosis sources, which included:

- 1) Sum of multiple isotropic Gaussian diffusion components (Fig. 2A).
- 2) Sum of multiple uniformly oriented anisotropic Gaussian diffusion components with identical axial and radial diffusivities (Fig. 2B).
- 3) Single compartment with non-vanishing microscopic kurtosis (Fig. 2C).

Although in Fig. 2C1 a single component with positive μK is sketched as the extra-compartmental medium that encompasses randomly oriented anisotropic compartments, ground truth positive μK in both intra- and extra-“cellular” components can arise according to effective medium theory (84) due to, e.g., cross sectional size variance and packing degree (49,85–87). The exact μK value for a medium represented in Fig. 2C will depend on the volume fraction, anisotropy, size, and packing of the anisotropic compartments as well as on the acquisition parameters (87). To simplify, the DDE signal decay for the single isotropic compartment with positive microscopic kurtosis is here numerically computed using the signal representation $E(b_1, b_2) = \exp\left(-(b_1 + b_2)D + \frac{1}{6}(b_1^2 + b_2^2)D^2\mu K\right)$ with D and μK ground truth set to an arbitrary value of $0.65\mu\text{m}^2/\text{ms}$ and 1, respectively. Note that μK can also rise due to restricted diffusion. In section B of Supporting Information, simulations for diffusion inside spheres are also produced using the MISST package (88,89), which could represent neural soma (90) and other quasi-spherical objects such as boutons.

4) A system comprising different components and with non-zero contributions for all different kurtosis sources (Fig. 3A). For this system, we consider a sum of the compartment types used for the previous simulations with equal weights. As the mean diffusivities of the simulations 1, 2 and 3 are equal, this ensemble model can assess the robustness of estimates for different kurtosis sources individually by varying concrete model parameters. Given this, we then varied ground truth K_{iso} , ground truth K_{aniso} , and ground truth μK values. Please see the Supporting Information, Section A for full details on these simulations.

For all models, powder-averaged signals were generated for the four different sets of DDE acquisition parameters (c.f. Fig. 1) for total b-values $b_a = 2.5ms/\mu m^2$ (sets #1, #2, #3) and $b_b = 1ms/\mu m^2$ (set #4) ($\Delta = \tau_m = 12ms$ and $\delta = 3.5ms$ for all experiments) – note the maximum b-value of $2.5ms/\mu m^2$ was selected since this was showed to provide an optimal trend between signal contrast to measure diffusional kurtosis and minimization of biases from high order-terms (40). For all four sets, the 45 directions of a 3D spherical 8-design (91) were used for the single encoding of set #1 (Fig. 1, panel C1.2), for the double diffusion encodings of sets #2 and #4 (Fig. 1, panels C2.2 and C4.2), and for the first diffusion encoding of set #3 (Fig. 1, panels C3.2). The directions for the second diffusion encoding of set #3 were repeated for three equidistant orthogonal directions relative to each direction of the 3D spherical 8-design (Fig. 1, panels C3.2), yielding a total of 135 pairs of directions. To ensure homoscedasticity of powder-averaged signals, the acquisition of the 45 directions for sets #1, #2, and #4 were repeated three times ($45 \times 3 = 135$ pairs of directions).

For reference, signals were also produced for an adapted version of the previous (*old*) DDE protocol suggested for CTI (40). The b_1 , b_2 and θ values, as well as gradient directions schemes used for the improved (*new*) and *old* CTI protocols (CTI_{new} and CTI_{old}) are summarized in Table 1 (for more information on the *old* protocol, c.f. Supporting Information, Section C). In addition to the diffusion-weighted signals for the different CTI sets, 135 signal

replicas for $b_1 = b_2 = 0$ are incorporated in both protocols – this data is treated as an independent $b_t = 0$ set. To assess the robustness of estimates towards noise, all synthetic signals were corrupted by Rician noise with a nominal SNR of 40 before powder-averaging. Consideration about the precision of CTI for other SNR levels are discussed in Supporting Information, section D (c.f. Supporting Information Figure S3).

Table 1 – Summary of the DDE parameter combination used for the “new” CTI protocol (CTI_{new}) and the reference “old” CTI protocol (CTI_{old}). Parameters b_1 , b_2 , b_t are expressed in $ms/\mu m^2$.

<i>New CTI protocol – CTI_{new}</i>						
<i>set</i>	b_1	b_2	b_t	θ	b_Δ	direction scheme
<i>#1</i>	2.5	0	2.5	0°	1	45 directions of the 8-design (x3 repetitions)
<i>#2</i>	1.25	1.25	2.5	0°	1	45 directions of the 8-design (x3 repetitions) for both diffusion encodings
<i>#3</i>	1.25	1.25	2.5	90°	-1/2	45 directions of the 8-design for the 1 st encoding, repeated for 3 orthogonal directions for the 2 nd encoding
<i>#4</i>	0.5	0.5	1	0°	1	45 directions of spherical 8-design (x3 repetitions) for both diffusion encodings
<i>Old CTI protocol – CTI_{old}</i>						
<i>set</i>	b_1	b_2	b_t	θ	b_Δ	direction scheme
<i>#1</i>	2.5	0	2.5	0°	1	45 directions of the 8-design (x3 repetitions)
<i>#2</i>	2.5	2.5	5	0°	1	45 directions of the 8-design (x3 repetitions) for both diffusion encodings
<i>#3</i>	2.5	2.5	5	90°	-1/2	45 directions of the 8-design for the 1 st encoding, repeated for 3 orthogonal directions for the 2 nd encoding
<i>#4</i>	1	0	1	0°	1	45 directions of the 8-design (x3 repetitions)
<i>#5</i>	1	1	2	0°	1	45 directions of the 8-design (x3 repetitions) for both diffusion encodings
<i>#6</i>	1	1	2	90°	-1/2	45 directions of the 8-design for the 1 st encoding, repeated for 3 orthogonal directions for the 2 nd encoding

Data processing: CTI metrics were obtained by fitting Eq. 6 to the log of the powder-averaged signals of both *new* and *old* protocols using an ordinary linear-least-squares (OLLS) procedure. K_{aniso} , K_{iso} , and K_t were also estimated from the MGC approach by fitting Eq. 9 to the powder-average of CTI’s *new* protocol using an OLLS procedure. Mean and standard

deviation of each kurtosis estimates were computed by repeating simulations for 1000 iterations.

3.2. MRI experiments

All animal experiments were preapproved by the institutional and national authorities and carried out according to European Directive 2010/63. Data was acquired from N=3 female Long Evans rats (ages = 22/19/22 weeks old, weights = 354.6/260.4/334.5g in a 12 h/12 h light/dark cycle with ad libitum access to food and water) under anesthesia (~2.5% Isoflurane in 28% oxygen) using a 9.4T Bruker Biospec scanner equipped with an 86 mm quadrature transmission coil and 4-element array reception cryocoil.

Auxiliary sagittal T₂-weighted images were acquired using a RARE sequence (c.f. Supporting Information Section E for experimental parameters). Diffusion MRI datasets were then acquired using a DDE-EPI pulse sequence ($\Delta = \tau_m = 12$ ms, $\delta = 3.5$ ms) for 3 evenly spaced coronal slices placed using the sagittal T₂-weighted images as a reference (c.f. Supporting Information Figure S4). Per-slice respiratory gating was applied. These acquisitions followed the first CTI protocol reported in Table 1 along with 24 $b_t = 0$ acquisitions per DDE set. Other acquisition parameters included: TR/TE=3000/50.9 ms, in-plane resolution = 200×200 μm^2 , slice thickness = 0.9 mm acquisition bandwidth = 400 kHz, number of shots = 1, partial Fourier factor = 7/8 (partial Fourier acceleration=1.25). Acquisition time for the diffusion-weighted data was around 40 mins. To empirically check if our measurements satisfied the long mixing time regime, additional DDE data was acquired in rat #1 with parallel and antiparallel directions and an intermediate total b-value of $2\text{ms}/\mu\text{m}^2$ ($b_1 = b_2 = 1\text{ms}/\mu\text{m}^2$) (Supporting Information, section F).

Data-processing: C.f. Supporting Information Section G for full details. Briefly, data were denoised (92), Gibbs unring per channel (29,93), and the four channels were combined using sum-of-squares. Data were registered using a sub-pixel algorithm (94).

Both CTI and MGC approaches were used to provide kurtosis metrics by voxel-wise fitting of equations 6 and 9 to the set powder-averaged data (masked to avoid regions distorted due to b_0 inhomogeneities (Fig. 4A) using an OLS procedure. Moreover, for a quantitative analysis of the kurtosis sources, ten regions of interest (ROIs) were manually defined on the $b_t = 0$ images of rat #1, including the left and right cortical grey matter (GM), the right and left corpus callosum genu (CCg), the right and left corpus callosum body (CCb), the right and left corpus callosum splenium (CCs), and the right and left internal capsule (IC). To ensure consistency across animals, the ROIs for rats #2 and #3 were automatically generated for the other animals using non-parametric registration of fractional anisotropy maps (95,96).

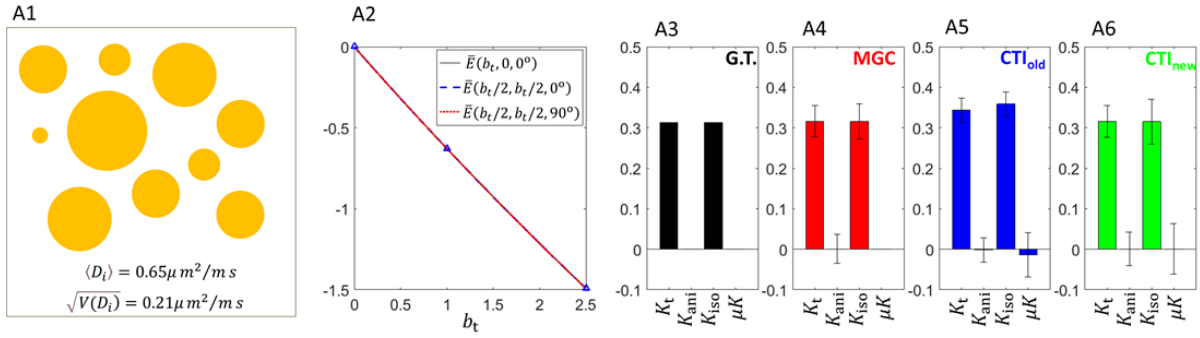
4. Results

4.1. Simulations

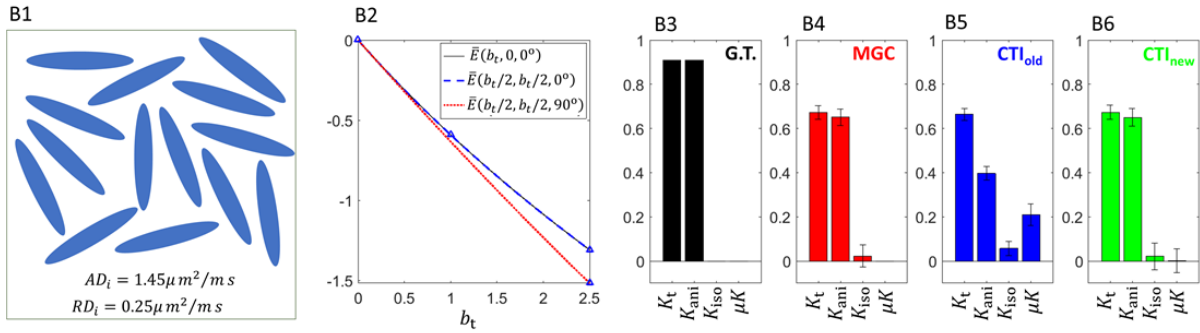
Figure 2 shows the simulation results for systems containing single component types (models 1-3). For isotropic Gaussian diffusion components with different mean diffusivities (Fig. 2A1), all DDE signal sets reveal identical log-signal dependencies with b_t (Fig. 2A2). The non-linearity of the log-signal decays was thus correctly identified as non-zero K_{iso} by all strategies (Fig. 2A3-6). For uniformly distributed anisotropic Gaussian components (Fig. 2B1), perpendicular DDE signals evidenced stronger diffusion-weighted attenuations, as expected (Fig. 2B2). The kurtosis estimated from MGC and the new CTI approaches was again correctly attributed to K_{aniso} (Fig. 2B4 and Fig. 2B6). Identically biased magnitudes were observed for both strategies for K_{aniso} likely due to higher-order-term biases which are expected to be larger for systems with high tissue dispersion (40). As expected, the old CTI protocol reports non-zero μK (Fig. 2B5), while the new CTI scheme corrects this bias and attributes a zero μK for such systems (Fig. 2B6).

For a system with microscopic disorder (Fig. 2C1, positive μK), asymmetric DDE signals (i.e., $\bar{E}_{DDE}(b_t, 0, 0^\circ)$) differ from their symmetric DDE counterparts (i.e. $\bar{E}_{DDE}(b_t/2, b_t/2, 0^\circ)$ and $\bar{E}_{DDE}(b_t/2, b_t/2, 90^\circ)$, Fig. 2C2). The finite μK strongly biases both K_{aniso} and K_{iso} from MGC (Fig. 2C4). On the other hand, CTI – both *old* and *new* protocols – correctly estimate the finite μK . These results are consistent for the non-vanishing (positive/negative) μK values of restricted diffusion inside spheres – see Supporting Information Figure S1.

A) Isotropic Gaussian diffusion components with different mean diffusivities



B) Evenly oriented anisotropic Gaussian diffusion components



C) Non-Gaussian diffusion due to microscopic disorder

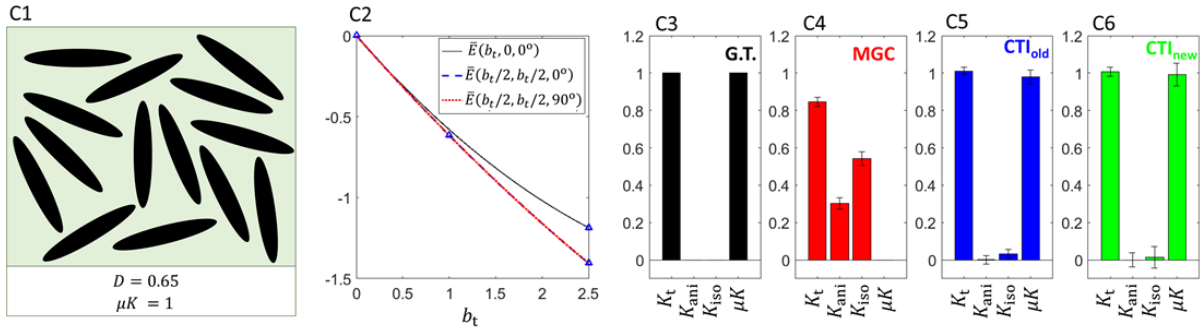


Figure 2 – Results for synthetic diffusion-weighted signals generated according to three systems containing single compartment types: **A)** Isotropic Gaussian diffusion components with different mean diffusivities sampled from a Gaussian distribution with mean $0.65 \mu\text{m}^2/\text{ms}$ and standard deviation $0.21 \mu\text{m}^2/\text{ms}$; **B)** Isotropically oriented anisotropic Gaussian diffusion components with axial and radial diffusivities of $1.45 \mu\text{m}^2/\text{ms}$ and $0.25 \mu\text{m}^2/\text{ms}$; **C)** Non-Gaussian diffusion due to microscopic disorder with ground truth $\mu K = 1$ and $D = 0.65 \mu\text{m}^2/\text{ms}$. From left to right, each panel shows: a schematic representation of the models (A1, B1, C1, D1); the signal decays for three different DDE experiment types in which signals of the improved CTI protocol are marked by the blue triangles (A2, B2, C2); the kurtosis ground truth values (A3, B3, C3); the kurtosis estimates obtained from MGC (A4, B4, C4); the kurtosis estimates obtained from the CTI using its previous “old” protocol (A5, B5, C5); the kurtosis estimates obtained from the CTI using its improved “new” protocol (A6, B6, C6). Note that when μK exists (panel C), the MGC approaches conflate μK with non-existing anisotropic and isotropic sources, while CTI clearly identifies the μK in the system. Also note that the new CTI protocol better resolves anisotropic and isotropic sources compared to its old counterpart (panels A and B).

In a realistic voxel, all kurtosis sources could exist simultaneously, and it is therefore instructive to assess whether the CTI framework can disentangle the kurtosis sources with specificity when all sources are present (Fig. 3). For this system, log-signal DDE decays are different for the three conditions (Fig. 3A2). The *new* CTI protocol successfully estimates the kurtosis sources (Fig. 3A3-6), while the *old* protocol overestimates μK .

We then investigated how changes in ground truth kurtosis sources would impact the different source estimates (see methods). Particularly, when changing the ground truth K_{iso} (Fig. 3B) or K_{aniso} (Fig. 3C), the new CTI and MGC approaches correctly show larger changes in K_{iso} and K_{aniso} respectively. The *old* CTI protocol has limited specificity for μK as varying K_{aniso} clearly affects μK . K_{aniso} and K_{iso} for the MGC approach also show limited specificity when the ground truth μK is varied (Fig. 3D).

Interestingly, we find that CTI *new* protocol correctly tracked the specific ground truth sources, i.e. major changes in improved CTI K_{iso} , K_{aniso} , and μK estimates are only observed when K_{iso} , K_{aniso} , and μK ground truths are varied, respectively (Fig. 3B3, Fig. 3C2, and Fig. 3D4), even if some offsets exist. Note that in Figure 3, due to the biases in MGC estimates introduced by μK , these only match the improved CTI estimates when ground truth μK is zero (c.f. Fig. 3D).

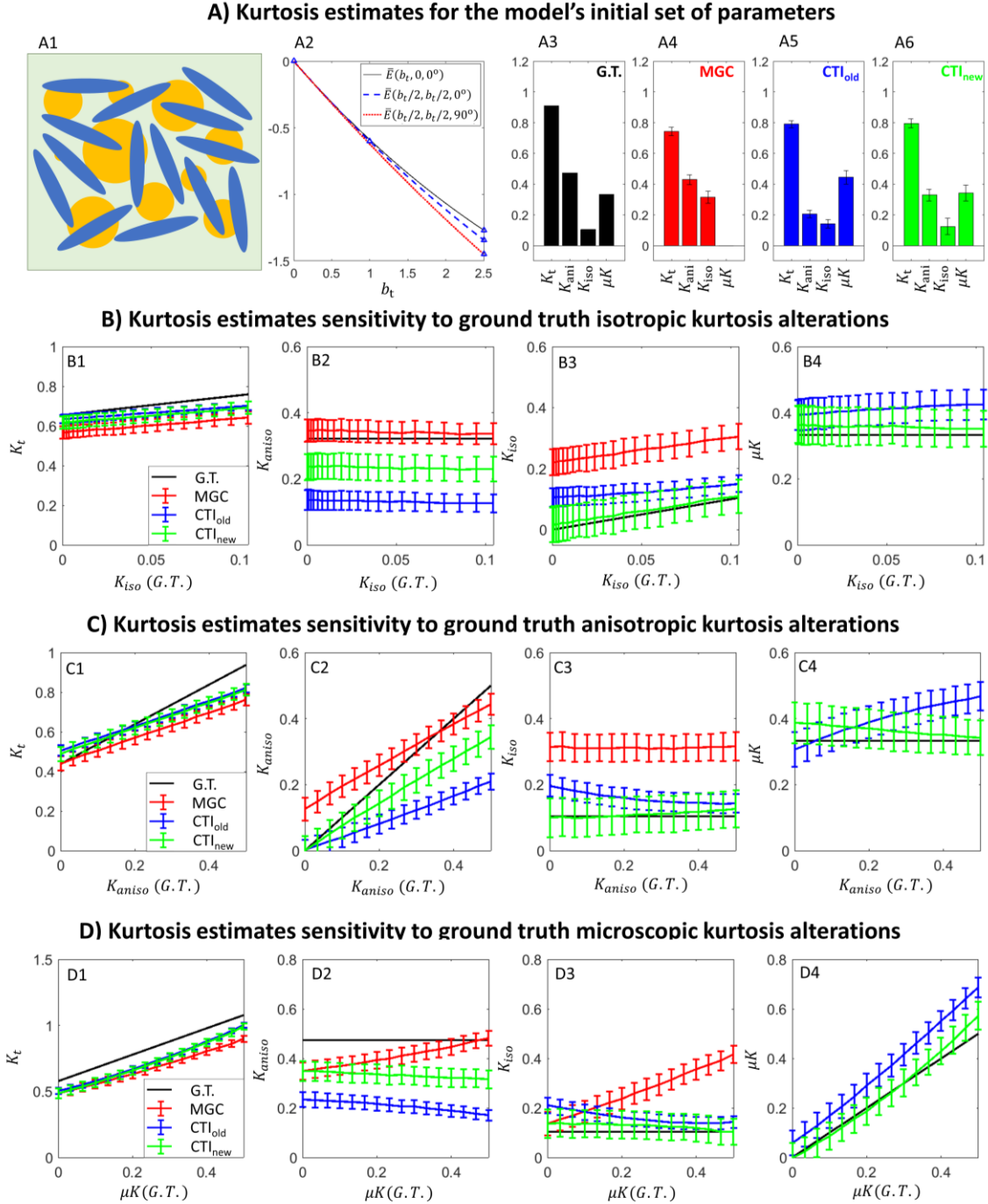


Figure 3 – Results for synthetic diffusion-weighted signals generated according to a system containing a sum of different compartment types (isotropic Gaussian + anisotropic Gaussian + isotropic non-Gaussian components): **A)** Results from the model's initial guess, i.e., isotropic components' mean diffusivities sampled from a Gaussian distribution with mean $0.65\mu\text{m}^2/\text{ms}$ and standard deviation $0.21\mu\text{m}^2/\text{ms}$, anisotropic Gaussian diffusion components with axial and radial diffusivities of $1.45\mu\text{m}^2/\text{ms}$ and $0.25\mu\text{m}^2/\text{ms}$; and non-Gaussian diffusion with $K_i = 1$ and $D_i = 0.65\mu\text{m}^2/\text{ms}$. **B)** CTI and MGC kurtosis estimates' sensitivity to ground truth K_{iso} alterations by changing the mean diffusivity variation of isotropic Gaussian components. **C)** CTI and MGC kurtosis estimates sensitivity to ground truth K_{aniso} alterations by changing the axial and radial diffusivities of anisotropic Gaussian compartments. **D)** CTI and MGC estimates sensitivity to ground truth μK alterations by changing the microscopic kurtosis level of the non-Gaussian component. These simulations suggest a very good stability for CTI (especially the new protocol), such that a change in one direction of any of the metrics will induce a systematically correct change in the estimated values.

4.2. MRI experiments

Coronal $b_t = 0$ images for all three rats are shown in Fig. 4A. Nominal SNR was ~ 30 for the raw data (Fig. 4B). Fig. 4C shows a representative diffusion-weighted image for a dMRI experiment acquired for the maximum b-value used on this study before and after PCA denoising. An SNR gain of ~ 1.3 was noted upon denoising (the nominal SNR of the denoised data was ~ 40).

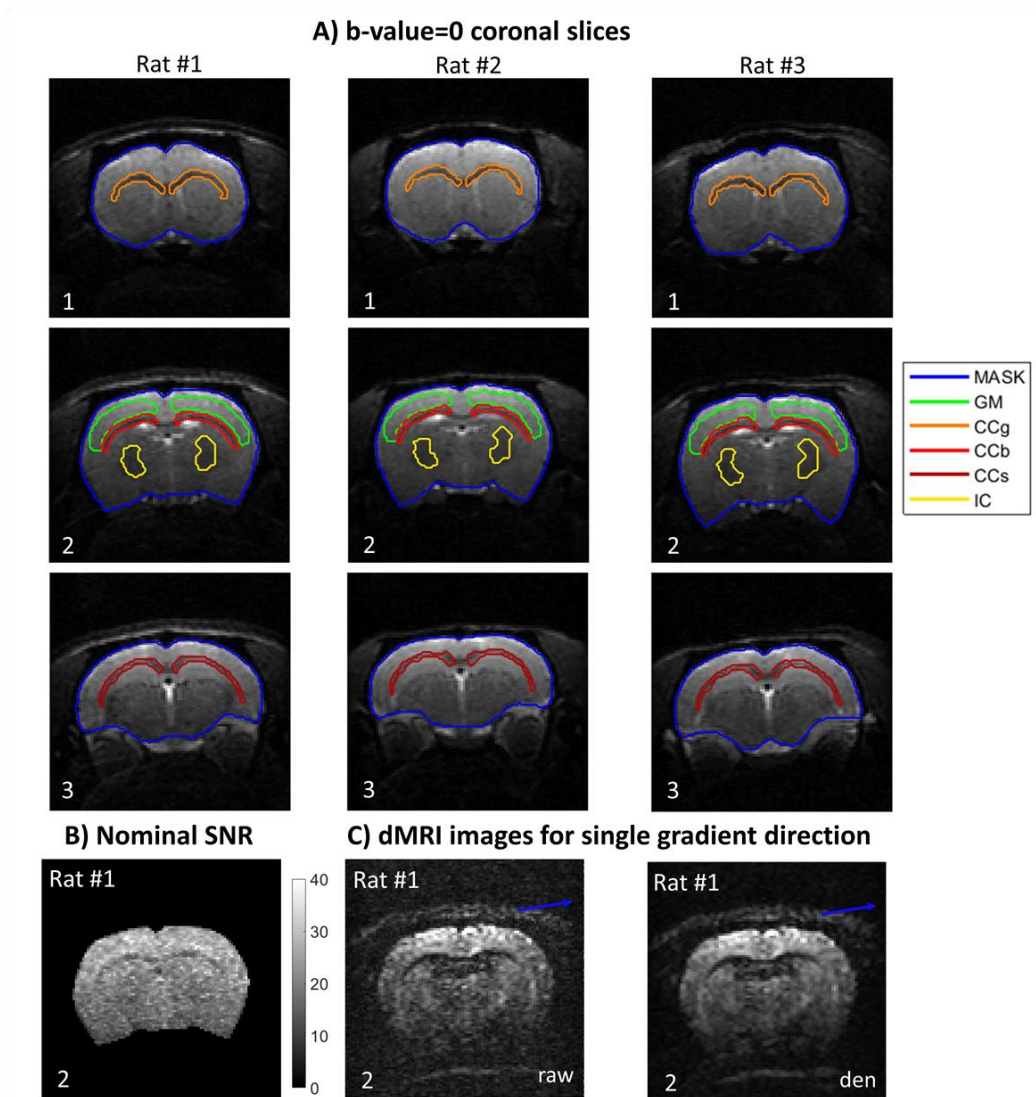


Figure 4 – Raw diffusion-weighted data: **A)** Representative $b_t = 0$ image for all animals and coronal slices and delineate regions of interest: brain mask (MASK); right and left cortical grey matter (GM); right and left corpus callosum genu (CCg); the right and left corpus callosum body (CCb); right and left corpus callosum splenium (CCs); and right and left internal capsule (IC). **B)** Representative nominal SNR map that was computed from all $b_t = 0$ acquisitions of Rat #1 and slice 2. **C)** Representative diffusion-weighted images (Rat #1, slice 2) for a single diffusion gradient direction (marked in blue) for the maximum total b_1 used in this study (i.e. $b_1 = 2.5 \mu\text{m}^2/\text{ms}$ and $b_2 = 0$) before and after PCA denoising (right and left respectively). Note the high signal to noise, and the lack of imaging artifacts.

Fig. 5A shows the powder-averaged signal decays for the four sets of the improved CTI protocol. The log difference between the powder-averaged data from set #1 and set #2 (Fig. 5B1) shows the sensitivity to μK (c.f. Eq. 4), while the log difference between the powder-averaged data from set #2 and set #3 (Fig. 5B4) shows CTI's sensitivity to K_{aniso} (c.f. Eq. 5). Positive log difference between set #1 and set #2, reveals a non-vanishing positive μK for both grey and white matter (c.f. Fig. 5B2 and Fig. 5B3).

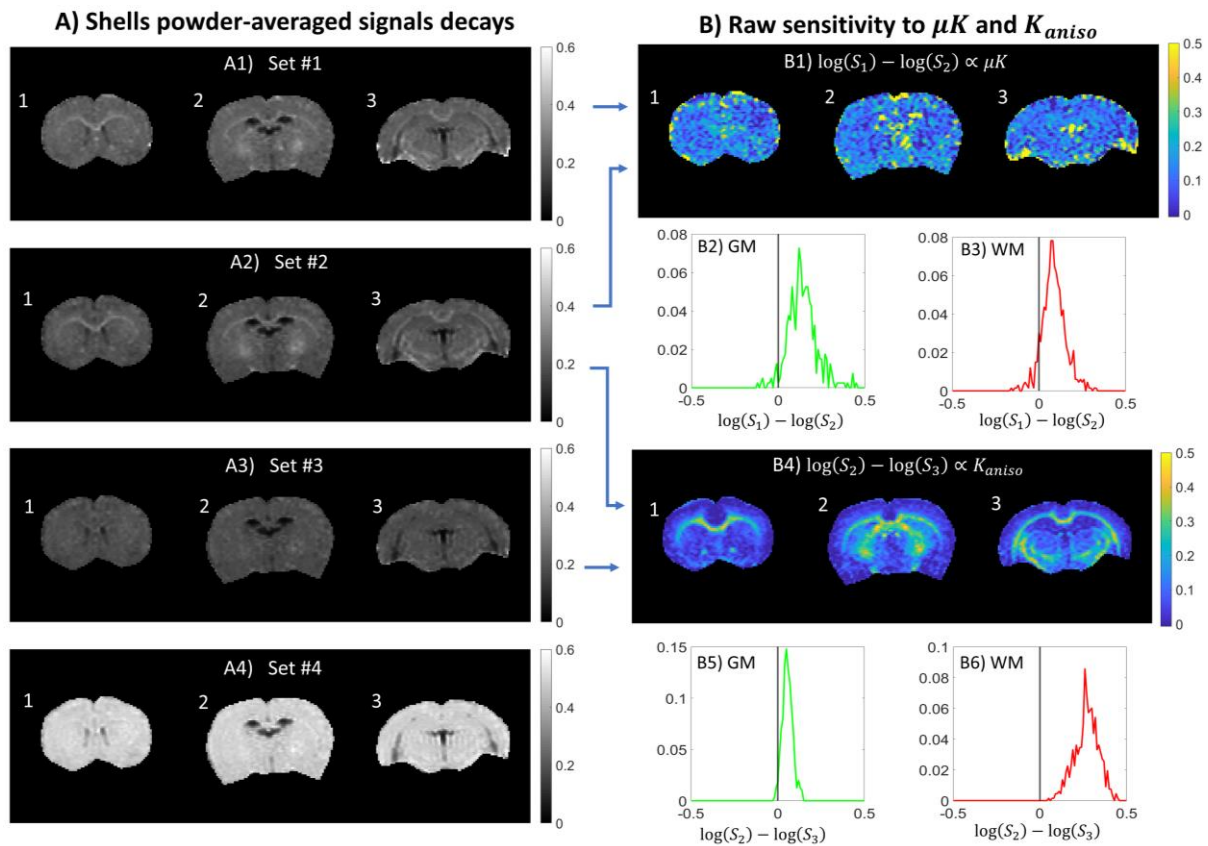


Figure 5 – Results from powder-averaged data for all slices of a representative animal (Rat #1). **A)** Powder-averaged signal decays for all four sets DDE experiments for CTI: set #1 (A1); set #2 (A2); set #3 (A3); and set #4 (A4); **B)** Raw sensitivity to microscopical kurtosis (μK) and anisotropic kurtosis (K_{aniso}): raw μK sensitivity maps are quantified by the log difference between powder-averaged signals of set #1 and #2 (B1); histogram of the log difference between powder-averaged signals of set #1 and #2 for all concatenated grey matter (GM) and white matter (WM) regions of interest (B2-3); raw K_{aniso} sensitivity maps are quantified by the log difference between powder-averaged signals of set #2 and #3 (B4); histogram of the log difference between powder-averaged signals of set #2 and #3 for all concatenated grey matter (GM) and white matter (WM) regions of interest (B5-6). Note that the data have sufficient power to resolve μK and K_{aniso} even for raw data itself.

The CTI kurtosis estimates for all slices of rat #1 and the second slice of rats #2 and #3 are shown in Fig. 6. Both K_t and K_{aniso} were higher in white matter regions (Fig. 6A-B). K_{iso} and μK maps show noisier spatial profiles than K_t and K_{aniso} maps (Fig. 6C-D). Nevertheless, μK shows to be a prevalent source of kurtosis, presenting higher values in grey matter and lower values in white matter (Fig. 6D, red arrows). The ROI analysis supported the trends observed in the kurtosis maps (Fig. 7A) – in general, μK shows to explain $64\pm 6\%$ and $30\pm 14\%$ of the total kurtosis in grey and white matter regions, respectively (Fig. 7, panel A4). The higher standard deviations for K_{iso} and μK is consistent with the lower precision observed in their maps (standard deviation of μK estimates are in line to the estimation error predicted in Supporting Information Figure S3). Fig. 7B shows the histograms of the different CTI-driven kurtosis estimates for combined grey and combined white matter ROIs. The mean values of grey and white matter are significantly different (two-sample t-test with unequal variances, $p < 0.001$ for kurtosis estimates and all three animals).

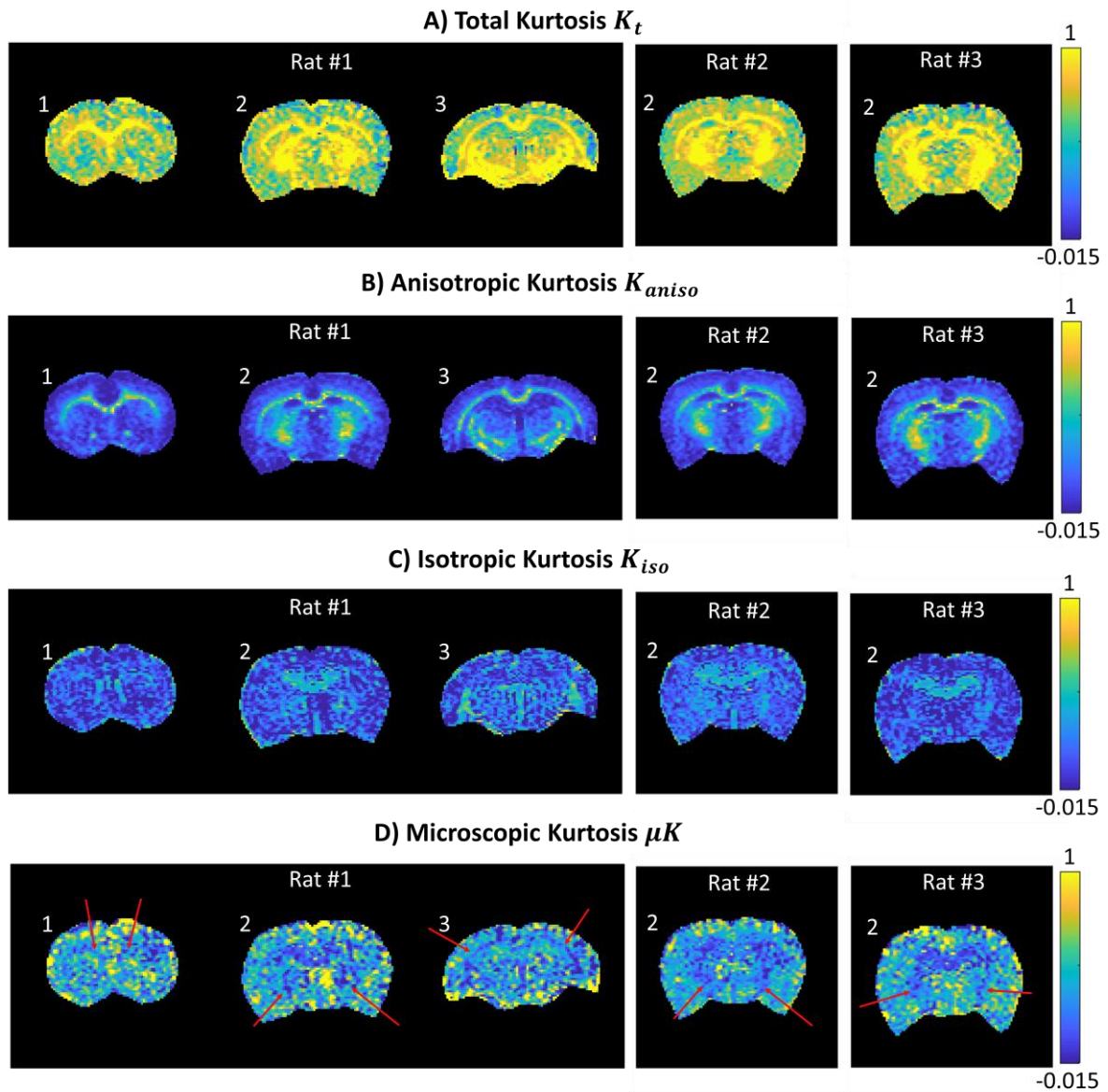


Figure 6 – Correlation Tensor Imaging kurtosis estimates. A) Total Kurtosis K_t ; **B)** Anisotropic Kurtosis K_{aniso} ; **C)** Isotropic Kurtosis K_{iso} ; **D)** Microscopic Kurtosis μK . The red arrow in panel D points to lower μK estimates observed particularly in white matter brain regions. On each panel, maps are presented for all slices of rat #1 and the 2nd slice of rats #2 and #3. Note how the total kurtosis maps, which have the largest values, are decomposed into their underlying sources. Anisotropic kurtosis is highest in WM, while isotropic kurtosis is highest in areas with larger partial volume effects between different diffusivities (namely areas with cerebrospinal fluid). Although the μK maps are slightly noisier, they do display GM/WM contrast.

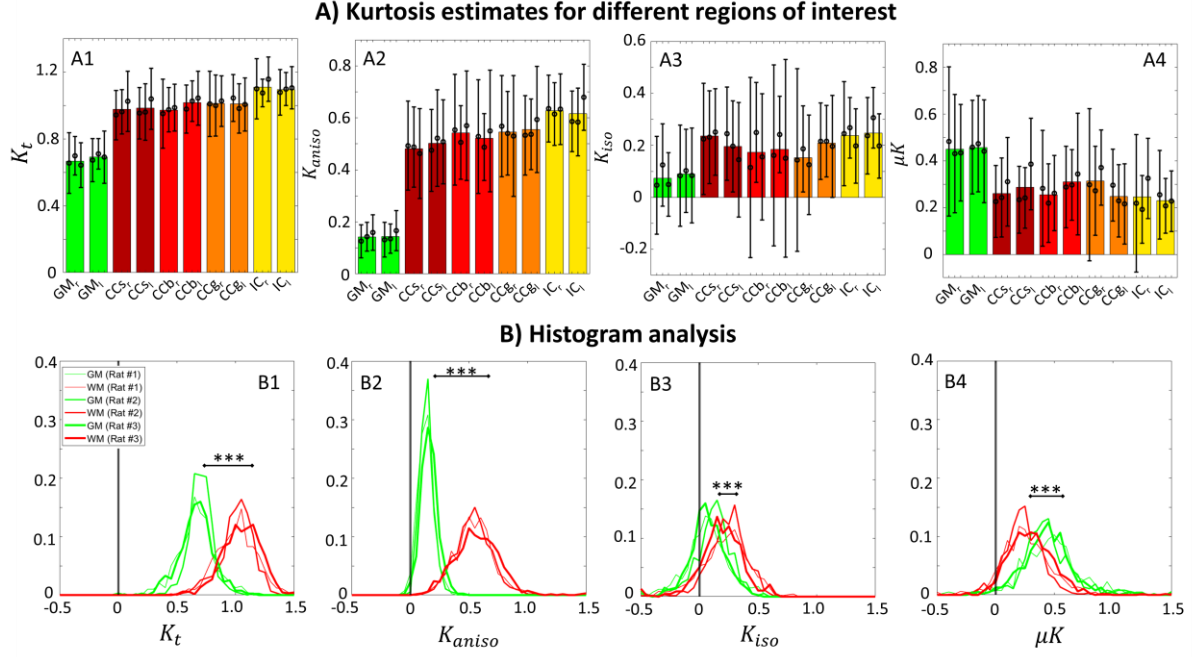


Figure 7 – Correlation Tensor Imaging kurtosis estimates in various brain regions. A) Mean and standard deviation of K_t (A1), K_{aniso} (A2), K_{iso} (A3), and μK (A4) estimates for different regions of interest – the three black intervals on each bar shows the mean and standard deviations for the three individual rats, while the coloured bars show the mean values across all three animals. Regions of interest for these panels include: the right and left cortical grey matter (GM_r and GM_l); the right and left corpus callosum splenium (CC_s_r and CC_s_l); the right and left corpus callosum body (CC_d_r and CC_d_l); the right and left corpus callosum genu (CC_g_r and CC_g_l); and the right and left internal capsule (IC_r and IC_l). **B)** Histograms of the K_t (B1), K_{aniso} (B2), K_{iso} (B3), and μK (B4) estimates for grey matter (histograms in green) and white matter (histograms in red) regions of interest - in each panel, the differences between the mean values from grey and white matter ROIs are statistically tested using a two-sampled t-test with unequal variances (* for $p < 0.05$, ** for $p < 0.01$, and *** for $p < 0.001$ ***). The histograms reveal that μK is in fact the dominant contributor to the total kurtosis in the GM.

We then turned to assess the impact of the finite μK on multiple gaussian component (MGC) analysis using only diffusion tensor variance. Figure 8A-C shows the kurtosis maps obtained from the MGC approach, while Figure 8D shows the histograms of MGC kurtosis values from white and grey matter ROIs. In comparison to their CTI counterparts, MGC-derived K_t was lower in both grey and white matter regions (Fig. 8A), while MGC K_{aniso} and K_{iso} values were higher. As for CTI, MGC mean K_t and K_{aniso} appear higher in white matter; however, non-significant differences between the white and grey matter voxels were observed for the MGC K_{iso} estimates (Fig. 8D3).

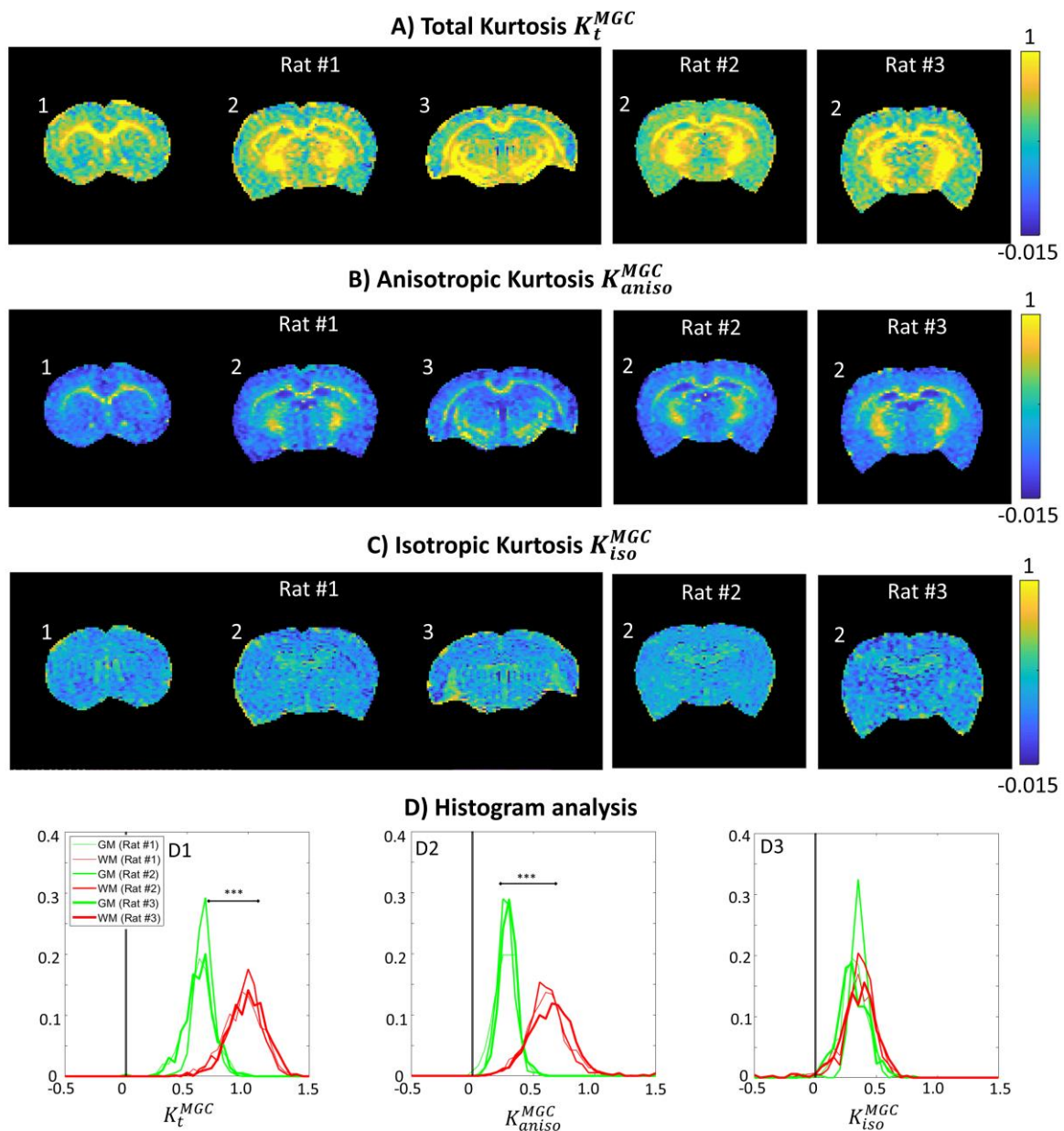


Figure 8 – Kurtosis estimates assuming multiple gaussian components (MGC). **A)** MGC total kurtosis (K_t^{MGC}) maps. **B)** MGC anisotropic kurtosis K_{aniso}^{MGC} maps. **C)** MGC isotropic kurtosis K_{iso}^{MGC} maps. **D)** Histograms of the K_t (D1), K_{aniso} (D2), and K_{iso} (D3) MGC estimates for all grey matter (histograms in green) and white matter (histograms in red) regions of interest – in each panel, the differences between the mean values of grey and white matter ROIs are statistically tested using a two-sampled t-test with unequal variances (* for $p < 0.05$, ** for $p < 0.01$, and *** for $p < 0.001$ ***). When forcing an MGC analysis on the data, the isotropic and anisotropic kurtosis metrics “absorb” the ignored μK , leading to biased maps (compare the MGC-driven maps in this Figure with those shown in Figure 6A-C, respectively, and the histograms in this figure with those shown in Figure 7B).

To further investigate the correlation between these metrics, scatter plots of MGC and CTI kurtosis estimates are shown in Fig. 9. Points in the scatter plots are color-coded according to CTI's microscopic kurtosis (μK) estimates, showing that higher differences between CTI and MGC estimates are associated with higher degrees of μK .

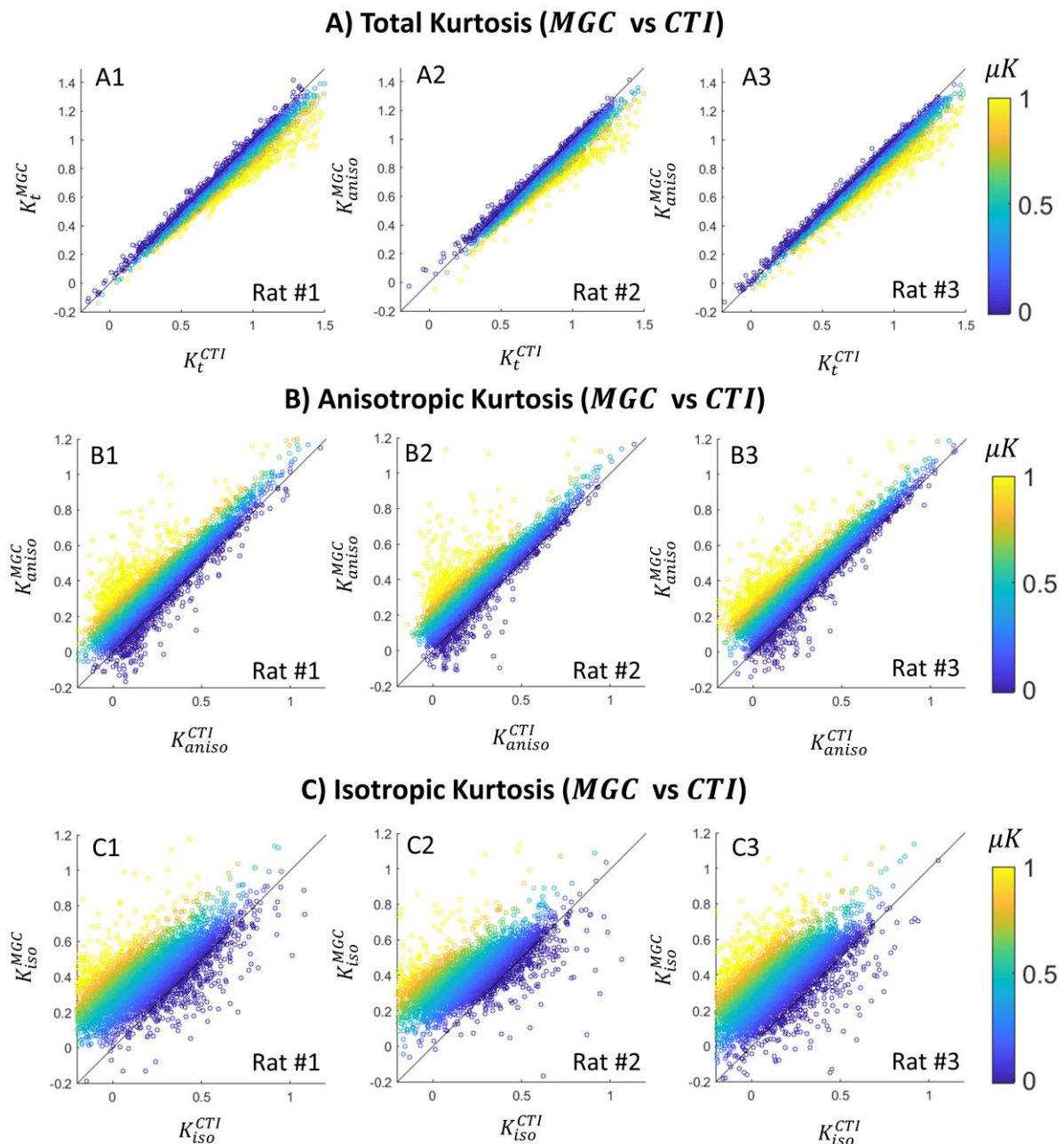


Figure 9 – Scatter plots between MGC and CTI estimates. A) Scatter plots between MGC total kurtosis (K_t^{MGC}) and CTI total kurtosis (K_t^{CTI}) estimates; B) Scatter plots between MGC anisotropic kurtosis (K_{aniso}^{MGC}) and CTI anisotropic kurtosis (K_{aniso}^{CTI}) estimates; C) Scatter plots between MGC isotropic kurtosis (K_{iso}^{MGC}) and CTI isotropic kurtosis (K_{iso}^{CTI}) estimates. Points in the scatter plots are colour coded according to CTI's microscopic kurtosis (μK) estimates. Note that as μK increases, the bias in the MGC estimates becomes more dramatic, especially for isotropic and anisotropic kurtosis sources.

5. Discussion

The conflation of underlying kurtosis sources in SDE was a major motivation in developing multidimensional diffusion encoding approaches. Even under the multiple gaussian component assumption, K_{aniso} and K_{iso} contrasts have shown great promise for e.g. distinguishing different tumor types and grades (39,72), depicting healthy and pathological age-related microstructural alterations (97), mapping multiple sclerosis lesions (98,99), and characterizing body organs (69,100). However, the MGC assumption implicitly ignores diffusion-time dependence (73,74) and μK effects, thereby risking the conflation of μK effects into the metrics. We therefore sought in this study to characterize the insofar ignored μK *in vivo* and assess its impact on the more conventional MGC approaches.

The Correlation Tensor Imaging (CTI) approach was recently introduced for μK mapping. CTI goes beyond the tensor-valued framework and simultaneously estimates K_{aniso} , K_{iso} , and μK – albeit at the expense of a larger number of acquisitions (40). The original CTI framework was lengthy and included DDE measurements that could bias μK in some scenarios (e.g., Fig. 2B5) due to higher order terms – a common issue for techniques based on the truncation of the signal cumulant expansion (40,77,101). To alleviate these drawbacks and accelerate the acquisitions, a new CTI strategy was here developed. We found a sparser set of DDE acquisitions for robustly resolving kurtosis sources and found that they can much more accurately estimate μK compared with the older protocol. By balancing the total b-values used for different DDE sets (c.f. Section C of the Supporting Information), the higher order term effects are greatly diminished (e.g. Fig. 2B6 and Fig. 3). The four CTI quantities (\bar{D} , K_{aniso} , K_{iso} , μK) can be fully resolved from only four different combinations of DDE parameters (b_1 , b_2 , θ) (c.f. DDE the sets in Fig. 1). In addition, we managed to accelerate CTI from 2h to under 40 mins, thereby making it applicable for *in vivo* preclinical and even clinical

mapping. It is interesting to note that μK alone can be estimated from the log signal differences of two different DDE experiments (c.f. Eq. 7), specifically using 1) parallel symmetric DDE gradient waveforms and 2) experiments analogous to SDE with the same total b-value, much like how microscopic anisotropy is estimated from parallel and perpendicular waveforms (54,55,57,76,77). Therefore, experiments aiming to resolve only μK could be even further accelerated.

In (40), we found significant positive μK estimates both in grey and white matter brain regions in the *in vivo* rat brain, suggesting it cannot be ignored in MGC approaches. Our new results with the improved CTI protocol confirmed the overall non-vanishing positive μK effects in both white and grey matter (Fig. 6, Fig. 7) and further highlighted significant μK differences between grey and white matter brain regions (Fig. 7). Positive μK is consistent with non-Gaussian diffusion effects due to intra-cellular cross-section size variance (18,49,86) and/or the presence of obstacles in tortuous extra-cellular environments (84,87). Therefore, the μK differences between grey and white matter could perhaps be explained by differences in both intra- and extra-cellular microstructural configurations (e.g. different compartmental cross sectional variance, different degree of cellular packing, etc.), or by the presence of a more negative μK contributions from restricted diffusion in white matter. Although μK will depend on a weighted sum of all above-mentioned effects, positive μK contributions are expected to prevail over negative μK contributions from completely restricted diffusion, as the latter are typically associated with low apparent diffusivities which strongly affects the signal contributed from these compartments (note that the total μK measured by CTI is a weighted average of all its contributions, where the weights depend on the squared apparent diffusivities of each contribution ($\mu K = \frac{\langle D_i^2 \mu K_i \rangle}{\bar{D}^2}$)).

Another significant result in this study, is that this non-vanishing μK can have a dramatic effect on kurtosis sources computed from tensor-valued and MGC framework (Fig. 8

and Fig. 9). In general, both K_{aniso} and K_{iso} derived from the MGC approach were biased towards higher values compared with their more accurate CTI counterparts. The color-coded scatter plots between MGC and CTI estimates revealed that differences can be fully explained by μK biases on MGC estimates (Fig. 9). It is important to note, that the influence of μK on K_{aniso} and K_{iso} can obscure microstructural differences, such as the K_{iso} differences between grey and white matter brain regions (Fig. 9).

5.1. Limitations and future work

Although it does not rely on the Gaussian diffusion assumption, CTI is still a cumulant expansion of DDE signals, which induces some implicit assumptions. Namely, disregarding higher-order cumulant terms; assuming the long mixing time regime (which can be empirically evaluated); and ignores exchange. Higher-order-term biases were here minimized by the new CTI protocol. The long mixing time regime effectively suppresses unwanted time-dependent diffusion correlations from the Q and S-tensors (60,80) and guarantees that the Z-tensor in Eq. 5 approaches the covariance tensor (40,60,76,80). This regime was empirically verified in acquired signals by measuring parallel and antiparallel DDE experiments and showing that they produce identical signal decays (55,57,59,102,103) (c.f., Supporting Information Figure S5). Lastly, since exchange is not explicitly modelled by CTI, it may affect the microscopic kurtosis metrics (19,42,104,105). Future studies will investigate the biological underpinning of microscopic kurtosis and how exchange between biological components can affect its estimates.

In this study, simple models were used to investigate the origin of CTI-driven kurtosis sources, and to illustrate the impact of finite μK on previous MGC approaches. These simple models are, however, are likely not sufficiently complex to fully represent biological tissues. Future studies should expand such in-silico experiments toward more complex simulations

allowing the assessment of the relationships between different kurtosis sources and concrete (sub)cellular features (e.g., cellular cross-sectional variance, cellular packing, exchange, etc.) (86,104,106–109). Another limitation of the current study is the reduced number of animals used. Although the power of measuring non-vanishing μK is ensured by using large ROIs (i.e., statistical power $\sim 100\%$ considering that μK is around 0.26 and 0.45 for ROIs containing more than 80 voxels and assuming that measures have a precision of ~ 0.2), future studies using a larger number of animals could be performed to explore for detailed regional differences of microscopic kurtosis.

Lundell et al. (2019) have recently shown that continuous diffusion gradient waveforms experiments probing identical b-tensors but different power spectra can provide different information about diffusion time-dependence and microscopic kurtosis (67). One could therefore argue MGC-driven biases could be reduced by adjusting the diffusion parameters of our CTI acquisition protocol, or by entirely excluding some acquisitions. In section H of Supporting Information, we report MGC kurtosis estimates obtained by fitting Eq. 9 to only DDE sets #2, #3, and #4, which correspond to an acquisition with identical waveform profiles. Under this condition, MGC K_{aniso} and CTI K_{aniso} are identical (c.f., Supporting Information Figure S6). However, the MGC K_{iso} estimates from this modified protocol are still a combination of isotropic and microscopic kurtosis effects. The comparison between CTI and MGC approaches could assist to define the regimes in which multidimensional MGC estimates are accurate.

Here, we managed to accelerate the CTI scan times to about 40 mins. Although this is still not (yet) sufficiently rapid for clinical translation, we note that the objective was only to identify the minimal acquisition set requirements for the extraction of all CTI quantities. Indeed, we acquired a large number of directions (135 per experiment set) to enhance the precision of our kurtosis estimates. In future studies, further acceleration could be obtained by

reducing the number of directions acquired for powder-averaging (78,99). We note that microscopic kurtosis can also be estimated directly from only 2 sets of this minimal protocol – albeit at the expense of not resolving K_{aniso} and K_{iso} – as was done for the raw μK sensitivity analysis in Fig. 5B. Future studies aiming to measure μK should also consider the desired estimation precision/accuracy when designing their experiments – some considerations on the relationship between μK precision and acquisition parameters are described in section D of the Supporting Information.

6. Conclusion

The accelerated Correlation Tensor Imaging approach developed here facilitated more accurate in-vivo acquisitions, and revealed that the commonly neglected μK is a significant source of total kurtosis in the brain, both in grey matter and in white matter. In fact, μK is the dominant kurtosis source in grey matter. Ignoring μK leads to significant bias in MGC approaches, underscoring the importance of accounting for μK in multidimensional diffusion encoding approaches. Our findings suggest promising new biomarkers in health and disease.

Acknowledgments

This study was funded by the European Research Council (ERC) (agreement No. 679058). The authors acknowledge the vivarium of the Champalimaud Centre for the Unknown, a facility of CONGENTO which is a research infrastructure co-financed by Lisboa Regional Operational Programme (Lisboa 2020), under the PORTUGAL 2020 Partnership Agreement through the European Regional Development Fund (ERDF) and Fundação para a Ciência e Tecnologia (Portugal), project LISBOA-01-0145-FEDER-022170.

References

1. Jones DK. Diffusion MRI : theory, methods, and applications. (Jones D, editor.) Oxford University Press; 2010.
2. Le Bihan D, Johansen-Berg H. Diffusion MRI at 25: exploring brain tissue structure and function. *Neuroimage* 2012;61:324–41 doi: 10.1016/j.neuroimage.2011.11.006.
3. Kiselev VG. Microstructure with diffusion MRI: what scale we are sensitive to? *J. Neurosci. Methods* 2021;347:108910 doi: 10.1016/j.jneumeth.2020.108910.
4. Stejskal EO, Tanner JE. Spin Diffusion Measurements: Spin Echoes in the Presence of a Time-Dependent Field Gradient. American Institute of Physics; 1965 pp. 288–292. doi: 10.1063/1.1695690.
5. Shemesh N, Jespersen SN, Alexander DC, et al. Conventions and nomenclature for double diffusion encoding NMR and MRI. *Magn. Reson. Med.* 2016;75:82–87 doi: 10.1002/mrm.25901.
6. Moseley ME, Kucharczyk J, Mintorovitch J, et al. Diffusion-weighted MR imaging of acute stroke: correlation with T2-weighted and magnetic susceptibility-enhanced MR imaging in cats. *AJNR. Am. J. Neuroradiol.* 1990;11:423–9.
7. Moseley ME, Cohen Y, Kucharczyk J, et al. Diffusion-weighted MR imaging of anisotropic water diffusion in cat central nervous system. *Radiology* 1990;176:439–445 doi: 10.1148/radiology.176.2.2367658.
8. Le Bihan D, Breton E, Lallemand D, Grenier P, Cabanis E, Laval-Jeantet M. MR imaging of intravoxel incoherent motions: application to diffusion and perfusion in neurologic disorders. *Radiology* 1986;161:401–407 doi: 10.1148/radiology.161.2.3763909.
9. Callaghan PT, Eccles CD, Xia Y. NMR microscopy of dynamic displacements: k-space and q-space imaging. *J. Phys. E.* 1988;21:820–822 doi: 10.1088/0022-3735/21/8/017.

10. Tuch DS, Reese TG, Wiegell MR, Van J. Wedeen. Diffusion MRI of Complex Neural Architecture. *Neuron* 2003;40:885–895 doi: 10.1016/S0896-6273(03)00758-X.
11. Wedeen VJ, Hagmann P, Tseng W-YI, Reese TG, Weisskoff RM. Mapping complex tissue architecture with diffusion spectrum magnetic resonance imaging. *Magn. Reson. Med.* 2005;54:1377–1386 doi: 10.1002/mrm.20642.
12. Özarslan E, Koay CG, Shepherd TM, et al. Mean apparent propagator (MAP) MRI: A novel diffusion imaging method for mapping tissue microstructure. *Neuroimage* 2013;78:16–32 doi: 10.1016/j.neuroimage.2013.04.016.
13. Basser PJ, Mattiello J, LeBihan D. MR diffusion tensor spectroscopy and imaging. *Biophys. J.* 1994;66:259–267 doi: 10.1016/S0006-3495(94)80775-1.
14. Pierpaoli C, Basser PJ. Toward a quantitative assessment of diffusion anisotropy. *Magn. Reson. Med.* 1996;36:893–906 doi: 10.1002/mrm.1910360612.
15. Basser PJ, Pierpaoli C. Microstructural and Physiological Features of Tissues Elucidated by Quantitative-Diffusion-Tensor MRI. *J. Magn. Reson. Ser. B* 1996;111:209–219 doi: 10.1006/jmrb.1996.0086.
16. Stepišnik J. Time-dependent self-diffusion by NMR spin-echo. *Phys. B Phys. Condens. Matter* 1993;183:343–350 doi: 10.1016/0921-4526(93)90124-O.
17. Gore JC, Xu J, Colvin DC, Yankeelov TE, Parsons EC, Does MD. Characterization of tissue structure at varying length scales using temporal diffusion spectroscopy. *NMR Biomed.* 2010;23:745–756 doi: 10.1002/nbm.1531.
18. Fieremans E, Burcaw LM, Lee H-H, Lemberskiy G, Veraart J, Novikov DS. In vivo observation and biophysical interpretation of time-dependent diffusion in human white matter. doi: 10.1016/j.neuroimage.2016.01.018.
19. Jensen JH, Helpert JA, Ramani A, Lu H, Kaczynski K. Diffusional kurtosis imaging: the quantification of non-gaussian water diffusion by means of magnetic resonance imaging.

- Magn. Reson. Imaging 2005;53 doi: 10.1002/mrm.20508.
20. Assaf Y, Basser PJ. Composite hindered and restricted model of diffusion (CHARMED) MR imaging of the human brain. *Neuroimage* 2005;27:48–58 doi: 10.1016/j.neuroimage.2005.03.042.
21. Jespersen SN, Kroenke CD, Østergaard L, Ackerman JJH, Yablonskiy DA. Modeling dendrite density from magnetic resonance diffusion measurements. *Neuroimage* 2007;34:1473–1486 doi: 10.1016/j.neuroimage.2006.10.037.
22. Assaf Y, Blumenfeld-Katzir T, Yovel Y, Basser PJ. Axcaliber: A method for measuring axon diameter distribution from diffusion MRI. *Magn. Reson. Med.* 2008;59:1347–1354 doi: 10.1002/mrm.21577.
23. Zhang H, Hubbard PL, Parker GJM, Alexander DC. Axon diameter mapping in the presence of orientation dispersion with diffusion MRI. *Neuroimage* 2011;56:1301–1315 doi: 10.1016/j.neuroimage.2011.01.084.
24. Zhang H, Schneider T, Wheeler-Kingshott CA, Alexander DC. NODDI: Practical in vivo neurite orientation dispersion and density imaging of the human brain. *Neuroimage* 2012;61:1000–1016 doi: 10.1016/j.neuroimage.2012.03.072.
25. Falangola MF, Jensen JH, Babb JS, et al. Age-related non-Gaussian diffusion patterns in the prefrontal brain. *J. Magn. Reson. Imaging* 2008;28:1345–1350 doi: 10.1002/jmri.21604.
26. Coutu JP, Chen JJ, Rosas HD, Salat DH. Non-Gaussian water diffusion in aging white matter. *Neurobiol. Aging* 2014;35:1412–1421 doi: 10.1016/j.neurobiolaging.2013.12.001.
27. Gong NJ, Wong CS, Chan CC, Leung LM, Chu YC. Aging in deep gray matter and white matter revealed by diffusional kurtosis imaging. *Neurobiol. Aging* 2014;35:2203–2216 doi: 10.1016/j.neurobiolaging.2014.03.011.
28. Price D, Tyler LK, Neto Henriques R, et al. Age-related delay in visual and auditory evoked responses is mediated by white- and grey-matter differences. *Nat. Commun.*

2017;8:15671 doi: 10.1038/ncomms15671.

29. Henriques RN. *Advanced Methods for Diffusion MRI Data Analysis and their Application to the Healthy Ageing Brain*. University of Cambridge; 2018. doi: <https://doi.org/10.17863/CAM.29356>.

30. Rudrapatna SU, Wieloch T, Beirup K, et al. Can diffusion kurtosis imaging improve the sensitivity and specificity of detecting microstructural alterations in brain tissue chronically after experimental stroke? Comparisons with diffusion tensor imaging and histology. *Neuroimage* 2014;97:363–373 doi: 10.1016/j.neuroimage.2014.04.013.

31. Hui ES, Fieremans E, Jensen JH, et al. Stroke Assessment With Diffusional Kurtosis Imaging. *Stroke* 2012;43:2968–2973 doi: 10.1161/STROKEAHA.112.657742.

32. Raab P, Hattingen E, Franz K, Zanella FE, Lanfermann H. Cerebral gliomas: Diffusional kurtosis imaging analysis of microstructural differences. *Radiology* 2010;254:876–881 doi: 10.1148/radiol.09090819.

33. Van Cauter S, Veraart J, Sijbers J, et al. Gliomas: Diffusion kurtosis MR imaging in grading. *Radiology* 2012;263:492–501 doi: 10.1148/radiol.12110927.

34. Abdalla G, Dixon L, Sanverdi E, et al. The diagnostic role of diffusional kurtosis imaging in glioma grading and differentiation of gliomas from other intra-axial brain tumours: a systematic review with critical appraisal and meta-analysis. *Neuroradiology* 2020;62:791–802 doi: 10.1007/s00234-020-02425-9.

35. Grossman EJ, Ge Y, Jensen JH, et al. Thalamus and cognitive impairment in mild traumatic brain injury: A diffusional kurtosis imaging study. *J. Neurotrauma* 2012;29:2318–2327 doi: 10.1089/neu.2011.1763.

36. Zhuo J, Xu S, Proctor JL, et al. Diffusion kurtosis as an in vivo imaging marker for reactive astrogliosis in traumatic brain injury. *Neuroimage* 2012;59:467–477 doi: 10.1016/j.neuroimage.2011.07.050.

37. Wang J-J, Lin W-Y, Lu C-S, et al. Parkinson Disease: Diagnostic Utility of Diffusion Kurtosis Imaging. *Radiology* 2011;261:210–217 doi: 10.1148/radiol.11102277.
38. Fieremans E, Benitez A, Jensen JH, et al. Novel White Matter Tract Integrity Metrics Sensitive to Alzheimer Disease Progression. *Am. J. Neuroradiol.* 2013;34:2105–2112 doi: 10.3174/ajnr.A3553.
39. Szczepankiewicz F, van Westen D, Englund E, et al. The link between diffusion MRI and tumor heterogeneity: Mapping cell eccentricity and density by diffusional variance decomposition (DIVIDE). *Neuroimage* 2016;142:522–532 doi: 10.1016/J.NEUROIMAGE.2016.07.038.
40. Henriques RN, Jespersen SN, Shemesh N. Correlation tensor magnetic resonance imaging. *Neuroimage* 2020;211:116605 doi: 10.1016/J.NEUROIMAGE.2020.116605.
41. Paulsen JL, Özarslan E, Komlosh ME, Basser PJ, Song Y-Q. Detecting compartmental non-Gaussian diffusion with symmetrized double-PFG MRI. *NMR Biomed.* 2015;28:1550–6 doi: 10.1002/nbm.3363.
42. Jensen JH, Helpert JA. MRI quantification of non-Gaussian water diffusion by kurtosis analysis. *NMR Biomed.* 2010;23:698–710 doi: 10.1002/nbm.1518.
43. Fieremans E, Jensen JH, Helpert JA. White matter characterization with diffusional kurtosis imaging. *Neuroimage* 2011;58:177–188 doi: 10.1016/j.neuroimage.2011.06.006.
44. Jespersen SN. White matter biomarkers from diffusion MRI. *J. Magn. Reson.* 2018;291:127–140 doi: 10.1016/j.jmr.2018.03.001.
45. Novikov DS, Veraart J, Jelescu IO, Fieremans E. Rotationally-invariant mapping of scalar and orientational metrics of neuronal microstructure with diffusion MRI. *Neuroimage* 2018;174:518–538 doi: 10.1016/j.neuroimage.2018.03.006.
46. Lampinen B, Szczepankiewicz F, Mårtensson J, van Westen D, Sundgren PC, Nilsson M. Neurite density imaging versus imaging of microscopic anisotropy in diffusion MRI: A

- model comparison using spherical tensor encoding. *Neuroimage* 2017;147:517–531 doi: 10.1016/j.neuroimage.2016.11.053.
47. Lampinen B, Szczepankiewicz F, Novén M, et al. Searching for the neurite density with diffusion MRI: Challenges for biophysical modeling. *Hum. Brain Mapp.* 2019;40:2529–2545 doi: 10.1002/hbm.24542.
48. Henriques RN, Jespersen SN, Shemesh N. Microscopic anisotropy misestimation in spherical-mean single diffusion encoding MRI. *Magn. Reson. Med.* 2019;81:3245–3261 doi: 10.1002/mrm.27606.
49. Dhital B, Kellner E, Kiselev VG, Reisert M. The absence of restricted water pool in brain white matter. *Neuroimage* 2018;182:398–406 doi: 10.1016/j.neuroimage.2017.10.051.
50. Jelescu IO, Palombo M, Bagnato F, Schilling KG. Challenges for biophysical modeling of microstructure. *J. Neurosci. Methods* 2020;344:108861 doi: 10.1016/j.jneumeth.2020.108861.
51. Topgaard D. Multidimensional diffusion MRI. *J. Magn. Reson.* 2017;275:98–113 doi: 10.1016/J.JMR.2016.12.007.
52. Szczepankiewicz F, Westin CF, Nilsson M. Gradient waveform design for tensor-valued encoding in diffusion MRI. *J. Neurosci. Methods* 2020;348:109007 doi: 10.1016/j.jneumeth.2020.109007.
53. Henriques RN, Palombo M, Jespersen SN, Shemesh N, Lundell H, Ianaş A. Double diffusion encoding and applications for biomedical imaging. *J. Neurosci. Methods* 2020 doi: 10.1016/j.jneumeth.2020.108989.
54. Cory DG, Garroway AN, Miller JB. Applications of spin transport as a probe of local geometry. *Polym Prepr* 1990;31:149.
55. Mitra PP. Multiple wave-vector extensions of the NMR pulsed-field-gradient spin-echo diffusion measurement. *Phys. Rev. B* 1995;51:15074–15078 doi:

10.1103/PhysRevB.51.15074.

56. Wong EC, Cox RW, Song AW. Optimized isotropic diffusion weighting. *Magn. Reson. Med.* 1995;34:139–143 doi: 10.1002/mrm.1910340202.

57. Ozarslan E. Compartment shape anisotropy (CSA) revealed by double pulsed field gradient MR. *J. Magn. Reson.* 2009;199:56–67 doi: 10.1016/j.jmr.2009.04.002.

58. Shemesh N, Özarslan E, Bar-Shir A, Basser PJ, Cohen Y. Observation of restricted diffusion in the presence of a free diffusion compartment: Single- and double-PFG experiments. *J. Magn. Reson.* 2009;200:214–225 doi: 10.1016/j.jmr.2009.07.005.

59. Shemesh N, Özarslan E, Basser PJ, Cohen Y. Measuring small compartmental dimensions with low-q angular double-PGSE NMR: The effect of experimental parameters on signal decay. *J. Magn. Reson.* 2009;198:15–23 doi: 10.1016/j.jmr.2009.01.004.

60. Jespersen SN, Buhl N. The displacement correlation tensor: Microstructure, ensemble anisotropy and curving fibers. *J. Magn. Reson.* 2011;208:34–43 doi: 10.1016/j.jmr.2010.10.003.

61. Lawrenz M, Koch MA, Finsterbusch J. A tensor model and measures of microscopic anisotropy for double-wave-vector diffusion-weighting experiments with long mixing times. *J. Magn. Reson.* 2010;202:43–56 doi: 10.1016/j.jmr.2009.09.015.

62. Hui ES, Jensen JH. Double-pulsed diffusional kurtosis imaging for the in vivo assessment of human brain microstructure. *Neuroimage* 2015;120:371–381 doi: 10.1016/j.neuroimage.2015.07.013.

63. Topgaard D. Isotropic diffusion weighting in PGSE NMR: Numerical optimization of the q-MAS PGSE sequence. *Microporous Mesoporous Mater.* 2013;178:60–63 doi: 10.1016/j.micromeso.2013.03.009.

64. Eriksson S, Lasic S, Topgaard D. Isotropic diffusion weighting in PGSE NMR by magic-angle spinning of the q-vector. *J. Magn. Reson.* 2013;226:13–18 doi:

10.1016/j.jmr.2012.10.015.

65. Lasič S, Szczepankiewicz F, Eriksson S, Nilsson M, Topgaard D. Microanisotropy imaging: quantification of microscopic diffusion anisotropy and orientational order parameter by diffusion MRI with magic-angle spinning of the q-vector. *Front. Phys.* 2014;2:11 doi: 10.3389/fphy.2014.00011.

66. Sjölund J, Szczepankiewicz F, Nilsson M, Topgaard D, Westin C-F, Knutsson H. Constrained optimization of gradient waveforms for generalized diffusion encoding. *J. Magn. Reson.* 2015;261 doi: 10.1016/j.jmr.2015.10.012.

67. Lundell H, Nilsson M, Dyrby TB, et al. Multidimensional diffusion MRI with spectrally modulated gradients reveals unprecedented microstructural detail. *Sci. Rep.* 2019;9:1–12 doi: 10.1038/s41598-019-45235-7.

68. Szczepankiewicz F, Sjö Lund J, Ståhlberg F, Lä Tt J, Nilsson M. Tensor-valued diffusion encoding for diffusional variance decomposition (DIVIDE): Technical feasibility in clinical MRI systems. *PLoS One* 2019;14:e0214238 doi: 10.1371/journal.pone.0214238.

69. Lasič S, Szczepankiewicz F, Dall'Armellina E, et al. Motion-compensated b-tensor encoding for in vivo cardiac diffusion-weighted imaging. *NMR Biomed.* 2020;33 doi: 10.1002/nbm.4213.

70. Westin CF, Szczepankiewicz F, Pasternak O, et al. Measurement tensors in diffusion MRI: Generalizing the concept of diffusion encoding. In: *Lecture Notes in Computer Science (including subseries Lecture Notes in Artificial Intelligence and Lecture Notes in Bioinformatics)*. Vol. 8675 LNCS. Springer Verlag; 2014. pp. 209–216. doi: 10.1007/978-3-319-10443-0_27.

71. Szczepankiewicz F, Lasič S, van Westen D, et al. Quantification of microscopic diffusion anisotropy disentangles effects of orientation dispersion from microstructure: applications in healthy volunteers and in brain tumors. *Neuroimage* 2015;104:241–52 doi:

10.1016/j.neuroimage.2014.09.057.

72. Nilsson M, Szczepankiewicz F, Brabec J, et al. Tensor-valued diffusion MRI in under 3 minutes: An initial survey of microscopic anisotropy and tissue heterogeneity in intracranial tumors. *Magn. Reson. Imaging* 2020;83:608–620.

73. Jespersen SN, Olesen JL, Ianuş A, Shemesh N. Effects of nongaussian diffusion on “isotropic diffusion” measurements: An ex-vivo microimaging and simulation study. *J. Magn. Reson.* 2019;300:84–94 doi: 10.1016/J.JMR.2019.01.007.

74. Szczepankiewicz Filip, Lasic Samo, Nilsson Markus, Lundell Henrik, Westin Carl-Fredrik, Topgaard Daniel. Is spherical diffusion encoding rotation invariant? An investigation of diffusion time-dependence in the healthy brain. In: *ISMRM 27th Annual Meeting & Exhibition.* ; 2019.

75. Avram A V., Özarslan E, Sarlls JE, Basser PJ. In vivo detection of microscopic anisotropy using quadruple pulsed-field gradient (qPFG) diffusion MRI on a clinical scanner. *Neuroimage* 2013;64:229–239 doi: 10.1016/j.neuroimage.2012.08.048.

76. Jespersen SN, Lundell H, Sønderby CK, Dyrby TB. Orientationally invariant metrics of apparent compartment eccentricity from double pulsed field gradient diffusion experiments. *NMR Biomed.* 2013;26:1647–62 doi: 10.1002/nbm.2999.

77. Ianuş A, Jespersen SN, Serradas Duarte T, Alexander DC, Drobnjak I, Shemesh N. Accurate estimation of microscopic diffusion anisotropy and its time dependence in the mouse brain. *Neuroimage* 2018;183:934–949 doi: 10.1016/j.neuroimage.2018.08.034.

78. Kerkelä L, Henriques RN, Hall MG, Clark CA, Shemesh N. Validation and noise robustness assessment of microscopic anisotropy estimation with clinically feasible double diffusion encoding MRI. *Magn. Reson. Med.* 2020;83 doi: 10.1002/mrm.28048.

79. Cheng Y, Cory DG. Multiple Scattering by NMR. *J. Am. Chem. Soc.* 1999;121:7935–7936 doi: 10.1021/ja9843324.

80. Jespersen SN. Equivalence of double and single wave vector diffusion contrast at low diffusion weighting. *NMR Biomed.* 2012;25:813–818 doi: 10.1002/nbm.1808.
81. Ji Y, Paulsen J, Zhou IY, et al. In vivo microscopic diffusional kurtosis imaging with symmetrized double diffusion encoding EPI. *Magn. Reson. Med.* 2019;81:533–541 doi: 10.1002/mrm.27419.
82. Callaghan PT, Coy A, MacGowan D, Packer KJ, Zelaya FO. Diffraction-like effects in NMR diffusion studies of fluids in porous solids. *Nature* 1991;351:467–469 doi: 10.1038/351467a0.
83. Callaghan PT. Pulsed-Gradient Spin-Echo NMR for Planar, Cylindrical, and Spherical Pores under Conditions of Wall Relaxation. *J. Magn. Reson. Ser. A* 1995;113:53–59 doi: 10.1006/JMRA.1995.1055.
84. Novikov DS, Kiselev VG. Effective medium theory of a diffusion-weighted signal. *NMR Biomed.* 2010;23:682–697 doi: 10.1002/nbm.1584.
85. Burcaw LM, Fieremans E, Novikov DS. Mesoscopic structure of neuronal tracts from time-dependent diffusion. *Neuroimage* 2015;114:18–37 doi: 10.1016/j.neuroimage.2015.03.061.
86. Lee HH, Papaioannou A, Kim SL, Novikov DS, Fieremans E. A time-dependent diffusion MRI signature of axon caliber variations and beading. *Commun. Biol.* 2020;3:1–13 doi: 10.1038/s42003-020-1050-x.
87. Lee HH, Papaioannou A, Novikov DS, Fieremans E. In vivo observation and biophysical interpretation of time-dependent diffusion in human cortical gray matter. *Neuroimage* 2020;222:117054 doi: 10.1016/j.neuroimage.2020.117054.
88. Drobnjak I, Zhang H, Hall MG, Alexander DC. The matrix formalism for generalised gradients with time-varying orientation in diffusion NMR. *J. Magn. Reson.* 2011;210:151–157 doi: 10.1016/j.jmr.2011.02.022.

89. Ianuș A, Alexander DC, Drobňjak I. Microstructure imaging sequence simulation toolbox. In: Lecture Notes in Computer Science (including subseries Lecture Notes in Artificial Intelligence and Lecture Notes in Bioinformatics). Vol. 9968 LNCS. Springer Verlag; 2016. pp. 34–44. doi: 10.1007/978-3-319-46630-9_4.
90. Claiborne BJ, Amaral DG, Cowan WM. Quantitative, three-dimensional analysis of granule cell dendrites in the rat dentate gyrus. *J. Comp. Neurol.* 1990;302:206–219 doi: 10.1002/cne.903020203.
91. Hardin RH, Sloane NJAA. McLaren’s improved snub cube and other new spherical designs in three dimensions. *Discret. Comput. Geom.* 1996;15:429–441 doi: 10.1007/BF02711518.
92. Veraart J, Novikov DS, Christiaens D, Ades-aron B, Sijbers J, Fieremans E. Denoising of diffusion MRI using random matrix theory. *Neuroimage* 2016;142:394–406 doi: 10.1016/j.neuroimage.2016.08.016.
93. Kellner E, Dhital B, Kiselev VG, Reiser M. Gibbs-ringing artifact removal based on local subvoxel-shifts. *Magn. Reson. Med.* 2016;76:1574–1581 doi: 10.1002/mrm.26054.
94. Guizar-Sicairos M, Thurman ST, Fienup JR. Efficient subpixel image registration algorithms. *Opt. Lett.* 2008;33:156–8.
95. Thirion JP. Image matching as a diffusion process: An analogy with Maxwell’s demons. *Med. Image Anal.* 1998;2:243–260 doi: 10.1016/S1361-8415(98)80022-4.
96. Vercauteren T, Pennec X, Perchant A, Ayache N. Diffeomorphic demons: efficient non-parametric image registration. *Neuroimage* 2009;45:S61–S72 doi: 10.1016/j.neuroimage.2008.10.040.
97. Kamiya K, Kamagata K, Ogaki K, et al. Brain White-Matter Degeneration Due to Aging and Parkinson Disease as Revealed by Double Diffusion Encoding. *Front. Neurosci.* 2020;14:1091 doi: 10.3389/fnins.2020.584510.

98. Andersen KW, Lasič S, Lundell H, et al. Disentangling white-matter damage from physiological fibre orientation dispersion in multiple sclerosis. *Brain Commun.* 2020;2 doi: 10.1093/braincomms/fcaa077.
99. Yang G, Tian Q, Leuze C, Wintermark M, McNab JA. Double diffusion encoding MRI for the clinic. *Magn. Reson. Med.* 2018;80:507–520 doi: 10.1002/mrm.27043.
100. Nery F, Szczepankiewicz F, Kerkelä L, et al. In vivo demonstration of microscopic anisotropy in the human kidney using multidimensional diffusion MRI. *Magn. Reson. Med.* 2019;82:2160–2168 doi: 10.1002/mrm.27869.
101. Chuhutin A, Hansen B, Jespersen SN. Precision and accuracy of diffusion kurtosis estimation and the influence of b-value selection. *NMR Biomed.* 2017;30 doi: 10.1002/NBM.3777.
102. Finsterbusch J. Extension of the double-wave-vector diffusion-weighting experiment to multiple concatenations. *J. Magn. Reson.* 2009;198:174–182 doi: 10.1016/j.jmr.2009.02.003.
103. Finsterbusch J. The parallel-antiparallel signal difference in double-wave-vector diffusion-weighted MR at short mixing times: A phase evolution perspective. *J. Magn. Reson.* 2011;208:114–121 doi: 10.1016/j.jmr.2010.10.012.
104. Fieremans E, Novikov DS, Jensen JH, Helpert JA. Monte Carlo study of a two-compartment exchange model of diffusion. *NMR Biomed.* 2010;23:711–24 doi: 10.1002/nbm.1577.
105. Ning L, Nilsson M, Lasič S, Westin C-F, Rathi Y. Cumulant expansions for measuring water exchange using diffusion MRI. *J. Chem. Phys.* 2018;148:074109 doi: 10.1063/1.5014044.
106. Skinner NP, Kurpad SN, Schmit BD, Budde MD. Detection of acute nervous system injury with advanced diffusion-weighted MRI: A simulation and sensitivity analysis. *NMR Biomed.* 2015;28:1489–1506 doi: 10.1002/nbm.3405.

107. Fieremans E, Lee HH. Physical and numerical phantoms for the validation of brain microstructural MRI: A cookbook. *Neuroimage* 2018;182:39–61 doi: 10.1016/j.neuroimage.2018.06.046.
108. Palombo M, Alexander DC, Zhang H. A generative model of realistic brain cells with application to numerical simulation of the diffusion-weighted MR signal. *Neuroimage* 2019;188:391–402 doi: 10.1016/j.neuroimage.2018.12.025.
109. Callaghan R, Alexander DC, Palombo M, Zhang H. ConFiG: Contextual Fibre Growth to generate realistic axonal packing for diffusion MRI simulation. *Neuroimage* 2020;220:117107 doi: 10.1016/j.neuroimage.2020.117107.

Supporting Information

Section A – Simulation details (Methods)

To assess the robustness of the different kurtosis source estimation strategies (MGC and CTI), we harnessed details simulations for the following scenarios:

5) Sum of multiple isotropic Gaussian diffusion components with mean diffusivities D_i sampled from a Gaussian distribution with mean $\langle D_i \rangle = 0.65\mu\text{m}^2/\text{ms}$ and standard deviation $\sqrt{V(D_i)} = 0.21\mu\text{m}^2/\text{ms}$ (Fig. 2A). Ground truth parameters for this model are: $D = 0.65\mu\text{m}^2/\text{ms}$, $K_t = K_{iso} = 0.31$, $K_{aniso} = \mu K = 0$.

6) Sum of multiple uniformly oriented anisotropic Gaussian diffusion components all with the same axial and radial diffusivities of $AD_i = 1.45\mu\text{m}^2/\text{ms}$ and $RD_i = 0.25\mu\text{m}^2/\text{ms}$ (Fig. 2B). Ground truth parameters for this model are: $D = 0.65\mu\text{m}^2/\text{ms}$, $K_t = K_{aniso} = 0.91$, $K_{iso} = \mu K = 0$.

7) Single compartment with positive source of microscopic kurtosis. According to the effective medium theory (84), compartments with microscopic disorder can exhibit non-Gaussian diffusion with a positive microscopic kurtosis contribution μK_i (84,85)). Although in Fig. 2C a single component with positive μK is sketched as an extra-compartmental medium that encompasses randomly oriented anisotropic compartments, microstructural disorder in both intra- and extra-“cellular” components arising, e.g., due to cross sectional size variance and packing degree (49,85–87). The exact μK value for a medium represented in Fig. 2C will depend on the volume fraction, anisotropy, size, and packing of the anisotropic compartments as well as on the acquisition parameters (87). To simplify, the DDE signal decay for the single isotropic compartment with positive microscopic kurtosis is here numerically computed using the signal representation $E(b_1, b_2) = \exp\left(- (b_1 + b_2)D + \frac{1}{6}(b_1^2 + b_2^2)D^2\mu K\right)$ with D and μK ground truth set to an arbitrary value of $0.65\mu\text{m}^2/\text{ms}$ and 1, respectively.

8) A system comprising different components and with non-zero contributions for all different kurtosis sources (Fig. 3A). For this system, we consider a sum of the compartment types used for the previous simulations with equal weights. The signal for this model is first computed with the diffusivity values specified above, resulting in the following ground truth parameters: $D = 0.65\mu\text{m}^2/\text{ms}$, $K_t = 0.911$, $K_{aniso} = 0.473$, $K_{iso} = 0.104$, and $\mu K = 0.333$. As the mean diffusivities of the simulations 1, 2 and 3 are equal, this ensemble model can assess the robustness of estimates for different kurtosis sources individually by varying concrete model parameters. In particular, different ground truth K_{iso} were generated by changing the mean diffusivity variance of Gaussian isotropic components $K_{iso}^{(g.t.)} = 3f_1V(D_i^{(1)})/D^2$; different ground truth K_{aniso} were created by changing the difference between the axial and radial diffusivities ($\alpha = AD_i^{(2)} - RD_i^{(2)}$) of uniformly oriented anisotropic Gaussian components $K_{aniso}^{(g.t.)} = 4f_2\alpha^2/15D^2$. In the latter case, $AD_i^{(2)}$ and $RD_i^{(2)}$ were computed as $D + 2\alpha/3$ and $D - \alpha/3$ for α values sampled from 0 to $1.95\mu\text{m}^2/\text{ms}$ to keep the mean diffusivity constant. Finally, different ground truth μK values were generated by changing the microscopic kurtosis contribution of the non-Gaussian diffusion compartment $\mu K^{(g.t.)} = (1 - f_1 - f_2)\mu K^{(3)}$.

Section B – CTI in spherical compartments

The signals for restricted diffusion are produced using the MISST package (88, 89). These signals are first produced for a compartment radius of $3\ \mu\text{m}$ and intrinsic diffusivity of $2\ \mu\text{m}^2/\text{ms}$ (Supporting Information Figure S1 panel A). Note that these first simulations may represent, for example, small neural soma e.g. (90), and other smaller abundant quasi-spherical objects such as boutons.

In analogous to the system with microscopic disorder (Fig. 2C1), asymmetric DDE signals (i.e., $\bar{E}_{DDE}(b_t, 0, 0^\circ)$) for restricted diffusion differ from their symmetric DDE counterparts (i.e. $\bar{E}_{DDE}(b_t/2, b_t/2, 0^\circ)$ and $\bar{E}_{DDE}(b_t/2, b_t/2, 90^\circ)$, Supporting Information Fig. S1A2). Since these simulations comprise of a single isotropic compartment (where $K_t = \mu K$, and the other sources are identically zero), the respective microscopic kurtosis ground truth can be calculated from single diffusion encoding at single direction and multiple b-values using DKI. For this, synthetic signals for 26 evenly sampled b-values between 0 and $2.5\text{ms}/\mu\text{m}^2$ are generated (for $\Delta = 12\text{ms}$ and $\delta = 3.5\text{ms}$). Ground truth K_t and μK are shown in Supporting Information Fig. S1A3. MGC and CTI kurtosis estimates from the improved and old protocols are shown in Supporting Information Fig. S1A4-6. These panels show that CTI correctly estimate the finite μK , while the presence of negative μK biases both K_{aniso} and K_{iso} from MGC.

Restricted diffusion simulations are then expanded to spherical compartment with varying angles. Panels B.1 and B.3 of Supporting Information Figure S1 shows the ground truths mean diffusivities and microscopic kurtosis as a function of the radius of the compartment. Synthetic signals for the CTI fitting are then sampled according to the improved protocol described on the main manuscript ($b_a = 2.5\text{ms}/\mu\text{m}^2$, $b_b = 1\text{ms}/\mu\text{m}^2$, $\Delta = t_m = 12\text{ms}$ and $\delta = 3.5\text{ms}$). To check for the long mixing time regime, we compare these signals with the signals generated by inverting the second gradient direction of the DDE experiments. Signal discrepancy between parallel and antiparallel signals were observed for spherical compartments for $r > 3\mu\text{m}$. Thus, to suppress diffusion time dependent effects on DDE signals, geometrically averaged signals are computed as $S_g = \sqrt{S_p S_a}$, where S_p and S_a are the signals of the improved protocol with non-inverted and inverted second gradient direction (note that this correction is not performed on the results of the main manuscript since the long mixing time regime was empirically shown to hold – see supporting information, section F). CTI mean

(C1), anisotropic kurtosis (C2), microscopic kurtosis (C3), and isotropic kurtosis (C4). Mean microscopic kurtosis estimates (B3) show analogous radius dependency than its ground truth (C3) and noise free values (C4). Lower precision in kurtosis estimates is, however, observed for lower radius which can be explained by higher estimate uncertainties of systems comprising lower diffusivities (c.f. supporting information, section D). As expected, mean isotropic and anisotropic kurtosis shows values close to zero (panels C2 and C4) – small deviations from zero at higher radius can be a consequence of higher-order terms biases, Rican noise biases, or incomplete Z tensor convergence to the covariance tensor (due to the violation of long mixing time regime).

Section C – Considerations for the “old” CTI approach

In our previous work (Henriques et al., 2020), kurtosis source estimates were derived from a CTI acquisition comprising six pairs of b_1 and b_2 combinations, repeated for 2 sets of parallel/perpendicular directions. These correspond to the 12 experiments summarized in Supporting Information Table S1.

Table S1 – Summary of the complete DDE parameter combination used for the CTI estimates in Henriques et al. (2020). The 12 parallel directions of the 5-design and the 60 perpendicular directions of Jespersen’s scheme are reported by (Jespersen et al., 2013).

<i>Complete non-optimized CTI protocol</i>						
<i>sets</i>	b_1	b_2	b_t	θ	b_Λ	direction scheme
#1	b_a	b_a	$2b_a$	0°	1	Parallel directions from 5-design and 8-design (12+45 directions)
#2	b_a	b_a	$2b_a$	90°	-1/2	Perpendicular directions of Jespersen’s DDE perpendicular scheme (60 directions)
#3	b_a	0	b_a	NA	1	Directions from 5-design and 8-design (12+45 directions)
#4	b_a	0	b_a	NA	1	1 st encoding directions of Jespersen’s perpendicular directions scheme (60 directions)
#5	0	b_a	b_a	NA	1	Directions from 5-design and 8-design (12+45 directions)
#6	0	b_a	b_a	NA	1	2 nd encoding directions of Jespersen’s perpendicular directions scheme (60 directions)
#7	b_b	b_b	$2b_b$	0°	1	Parallel directions from 5-design and 8-design (12+45 directions)
#8	b_b	b_b	$2b_b$	90°	-1/2	Perpendicular directions of Jespersen’s DDE perpendicular scheme (60 directions)
#9	b_b	0	b_b	NA	1	Directions from 5-design and 8-design (12+45 directions)
#10	b_b	0	b_b	NA	1	1 st encoding directions of Jespersen’s perpendicular directions scheme (60 directions)
#11	0	b_b	b_b	NA	1	Directions from 5-design and 8-design (12+45 directions)
#12	0	b_b	b_b	NA	1	2 nd encoding directions of Jespersen’s perpendicular directions scheme (60 directions)

It is important to note that in Henriques et al. (2020), sets #1, #2, #7 and #8 were also repeated for n_2 inverted directions to evaluate the long mixing time regime approximations. These inverted directions acquisitions are excluded in Supporting Information Table S1 for the sake of simplicity.

Note that this non-optimised protocol contains redundant sets. Particularly, sets #3-6 and sets #9-12 are related to identical powder-averaged signals, i.e. $\bar{E}_{DDE}(b_a, 0) = \bar{E}_{DDE}(0, b_a)$ and $\bar{E}_{DDE}(b_b, 0) = \bar{E}_{DDE}(0, b_b)$ respectively. For the reference non-optimized CTI protocol of our current study, these redundant sets are removed, and the direction schemes of each set are adapted to ensure homoscedasticity (Supporting Information Table S2).

Table S2 – Summary of the reference non-optimized CTI protocol used on the current study.

<i>Complete non-optimized CTI protocol</i>						
<i>sets</i>	\mathbf{b}_1	\mathbf{b}_2	\mathbf{b}_t	θ	\mathbf{b}_Λ	direction scheme
#1	b_a	0	b_a	NA	1	45 directions of the 8-design (x3 repetitions)
#2	b_a	b_a	$2b_a$	0°	1	45 directions of the 8-design (x3 repetitions) for both diffusion encodings
#3	b_a	b_a	$2b_a$	90°	-1/2	45 directions of the 8-design for the 1 st encoding, repeated for 3 orthogonal directions for the 2 nd encoding
#4	b_b	0	1	NA	1	45 directions of the 8-design (x3 repetitions)
#5	b_b	b_b	$2b_a$	0°	1	45 directions of the 8-design (x3 repetitions) for both diffusion encodings
#6	b_b	b_b	$2b_b$	90°	-1/2	45 directions of the 8-design for the 1 st encoding, repeated for 3 orthogonal directions for the 2 nd encoding

In contrast to the improved protocol of the current study, one can note that the non-optimized protocol presents set experiments with unbalanced total b-values, i.e. its symmetric DDE experiments (i.e. sets #2-3 and #5-6) are performed for a higher total b-value than SDE-equivalent experiments (i.e. sets #1 and #3).

To remain consistent with the improved protocol designed on our study, parameters b_a and b_b in Supporting Information Table S2 were set to $2.5\text{ms}/\mu\text{m}^2$ and $1\text{ms}/\mu\text{m}^2$ for the non-optimized protocol, which this led to a non-optimized protocol with a high total b-value of $5\text{ms}/\mu\text{m}^2$ (sets #2-3). In our previous work, we showed that higher b-values are associated with higher-order-term effects. However, here, we show that, rather of being only an effect of the higher b-values used, the biases in μK observed on our previous study is also a consequence of the unbalanced b-values used in the non-optimized protocol. Below, Supporting Information Figure S2 shows the simulation results for the non-optimized protocol for models 2 and 5 (models which showed to be problematic for the non-optimized protocol) applied with lower total b-values (i.e. $b_a = 1.25\text{ms}/\mu\text{m}^2$ and $b_b = 0.5\text{ms}/\mu\text{m}^2$), which still shows

overestimation of μK , thereby supporting the notion that unbalanced b-values contribute to the biases in μK estimation in the old CTI approach.

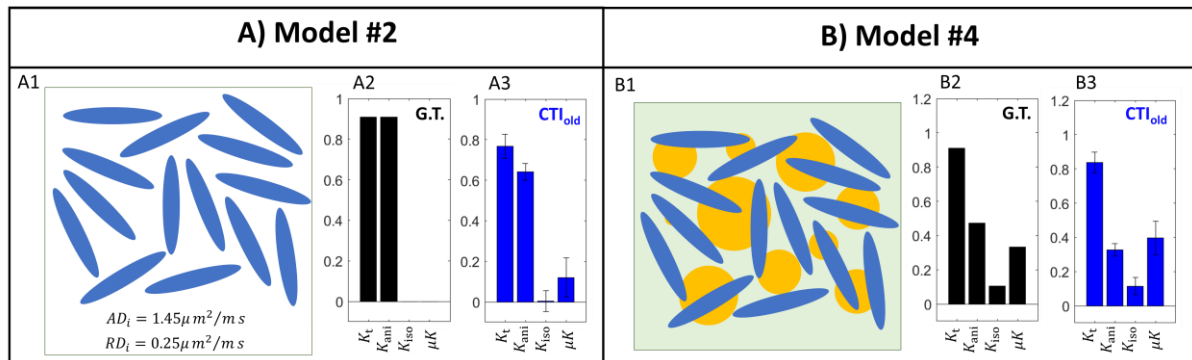


Figure S2 – Kurtosis estimates of non-optimized CTI protocol with parameters $b_a = 1.25 ms/\mu m^2$ and $b_b = 0.5 ms/\mu m^2$ for two simulations (model 2 and 4 described in main manuscript); A) Evenly oriented anisotropic Gaussian diffusion components; B) Sum of different compartment types (isotropic Gaussian + anisotropic Gaussian + isotropic non-Gaussian components). From left to right, each panel shows: a schematic representation of the toy models (A1, B1); the kurtosis ground truth values (A2, B2); and the kurtosis estimates obtained from the CTI using its “old” non-optimized protocol (A3, B3).

Section D - Precision of Microscopic Kurtosis estimates

Considering the propagation of uncertainty, the expected error of μK ($\sigma_{\mu K}$) can be calculated from Eq. 6, which yields:

$$\sigma_{\mu K} = \frac{12}{b_a^2 D^2} \sqrt{\frac{\sigma^2}{S_1^2 N} + \frac{\sigma^2}{S_2^2 N}} \quad (\text{S1})$$

where $S_1 = \bar{E}_{DDE}(b_a, 0)$, $S_2 = \bar{E}_{DDE}\left(\frac{b_a}{2}, \frac{b_a}{2}, 0^0\right)$, σ is the signal noise standard deviation, and N is the number of pairs of directions used to compute the powder averages (here we assumed that the error of the mean diffusivity D is negligible). From equation S1 one can note that $\sigma_{\mu K}$ does not only depend on acquisition parameters (b-value, number gradient direction pair) but on the ground truth diffusion parameters of the system (particularly, its mean diffusivity).

To illustrate the dependency of the μK uncertainty with the diffusion parameters of the system, Supporting Information Figure S3 panel A and B we shows the $\sigma_{\mu K}$ values computed for different ground truth mean diffusivities D and microscopic kurtosis μK based on the acquisition parameters of this study (i.e. $N=135$ and $b_a = 2.5\text{ms}/\mu\text{m}^2$) and for two different SNRs (40 and 20) - note, for this figure, ground truth S_1 and S_2 signals are approximated as $\bar{E}_{DDE}(b_1, b_2, 0^0) = \exp\left(-(b_1 + b_2)D + \frac{1}{6}(b_1^2 + b_2^2)D^2\mu K\right)$. These panels show that systems with lower mean diffusivities and microscopic kurtosis values are associated to lower μK uncertainties. For the mean diffusivity and microscopic kurtosis values observed on the white matter and grey matter ROIs of our study (marked in by the red and green points respectively), predicted $\sigma_{\mu K}$ are between 0.05 and 0.1 for a SNR=40 (Supporting Information Figure S3, panel A) and between 0.1 and 0.2 for a SNR=20 (Supporting Information Figure S3, panel A) – these uncertainly levels are in line with the standard deviation on panel A4 of Figure 7.

Panel C of Supporting Information Figure S3 shows the minimal SNR requirement to obtain a $\sigma_{\mu K}=0.05$, showing the high SNR requirements to estimate microscopic kurtosis for systems of low diffusivities. These SNR requirement maps was computed using the following expression for $N=135$ and $b_a = 2.5\text{ms}/\mu\text{m}^2$:

$$SNR = \frac{1}{\sigma_{\mu K}} \frac{12}{b_a^2 D^2} \sqrt{\frac{1}{S_1^2 N} + \frac{1}{S_2^2 N}} \quad (\text{S2})$$

Note that Supporting Information Figure S3 can be easily adapted to other acquisition parameters using equations S1 and S2.

To support that the propagation of uncertainty analysis is consistent to the numerical simulations, in Supporting Information Figure S3 panel D we show the histogram of μK estimates obtained from the main manuscript noise corrupted numerical simulations (signals from model 3 corrupted with Rician noise at a nominal SNR of 40) for three ground truth set of parameters representing: 1) a reference simulation with zero μK ($D_{gt} = 0.8\mu m^2/ms$, and $\mu K_{gt} = 0$); 2) the mean values measured for GM ($D_{gt} = 0.76\mu m^2/ms$, and $\mu K_{gt} = 0.45$); 3) the mean values measured for WM ($D_{gt} = 0.82\mu m^2/ms$, and $\mu K_{gt} = 0.27$). For these three sets of ground truth parameters, the standard deviation of the values reported in the histograms (0.067 ± 0.002 , 0.059 ± 0.002 , and 0.061 ± 0.002) are consistent to the $\sigma_{\mu K}$ values obtained for the propagation of uncertainty analysis (0.068, 0.055, 0.59). It is important to note that from our numerical simulations and propagation of uncertainty analysis, noise does introduce significant offset between the μK mean values and ground truth values and thus the measured positive μK values measured in our study cannot be explained as being a noise artifact.

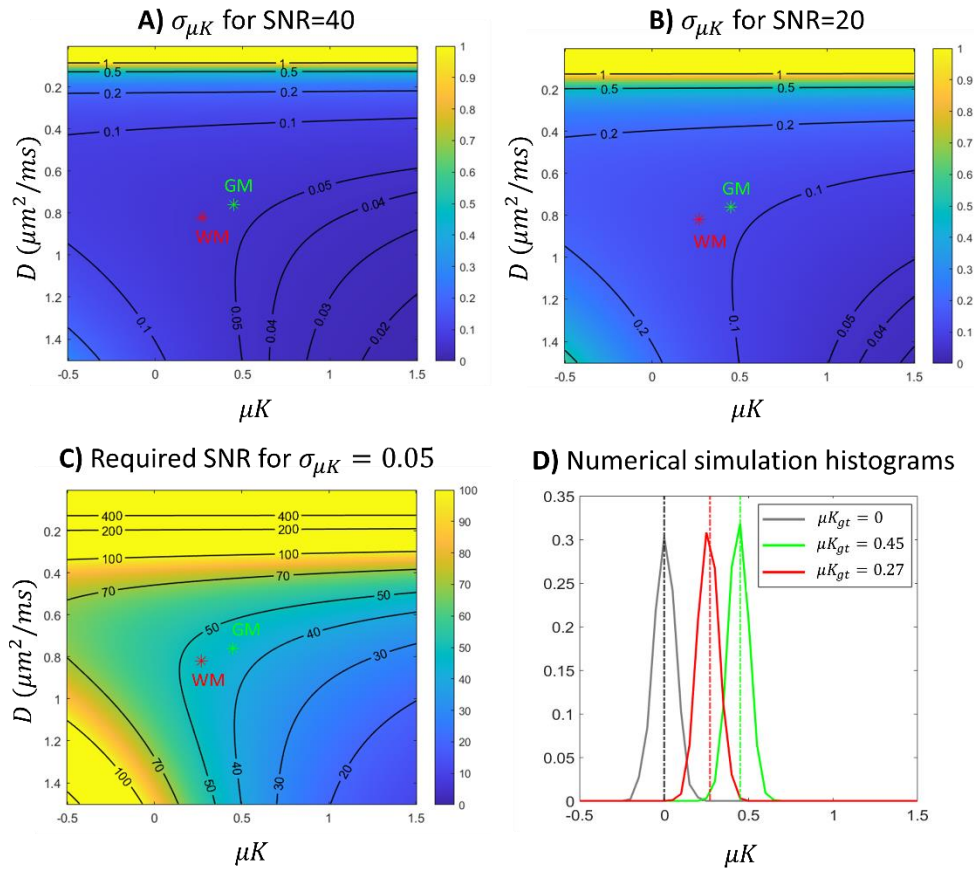


Figure S3 – Microscopic kurtosis estimation uncertainty. **A)** Microscopic kurtosis uncertainty $\sigma_{\mu K}$ prediction for different ground truth mean diffusivities D and microscopic kurtosis μK values and given the acquisition parameters of this study ($N=135$ and $b_a = 2.5\text{ms}/\mu\text{m}^2$) and a single acquisition nominal SNR of 40 (i.e. $\sigma = 0.025$); **B)** $\sigma_{\mu K}$ prediction for different ground truth D and μK values and given the acquisition parameters of this study ($N=135$ and $b_a = 2.5\text{ms}/\mu\text{m}^2$) and a single acquisition nominal SNR of 20 (i.e. $\sigma = 0.05$); **C)** Required SNR to obtain a $\sigma_{\mu K}=0.05$ and given the acquisition parameters of this study ($N=135$ and $b_a = 2.5\text{ms}/\mu\text{m}^2$). In all panels, the mean D and μK values observed on the white matter and grey matter ROIs of the rat brain data is marked in by the red and green points, respectively. **D)** histogram of μK estimates obtained from signals computed using numerical simulations (signals from model 3) and corrupted with Rician noise at a nominal SNR of 40 for three ground truth set of parameters representing: 1) $D_{gt} = 0.8\mu\text{m}^2/\text{ms}$, and $\mu K_{gt} = 0$ (histogram marked by the grey line); 2) $D_{gt} = 0.76\mu\text{m}^2/\text{ms}$, and $\mu K_{gt} = 0.45$ (histogram marked by the green line); 3) $D_{gt} = 0.82\mu\text{m}^2/\text{ms}$, and $\mu K_{gt} = 0.27$ (histograms marked by the red line). These latter histograms were produced for 1000 simulation iterations and the ground truth values are marked by the dashed lines.

Section E – Auxiliary T2-weighted experiments (Methods)

The T2 weighted images in this study were acquired with the following parameters: TR = 2000 ms, effective TE = 36 ms, RARE factor = 8, Field of View = $24 \times 16.1 \text{ mm}^2$, matrix size 160×107 , leading to an in-plane voxel resolution = $150 \times 150 \mu\text{m}^2$, slice thickness = $500 \mu\text{m}$ (21 slices), number of averages = 8. Representative raw sagittal T2-weighted images for all three rats are shown in Supporting Information Figure S4. These images were used as a reference for placing the 3 coronal slices for diffusion MRI acquisition – positions of the coronal slices are marked in red.

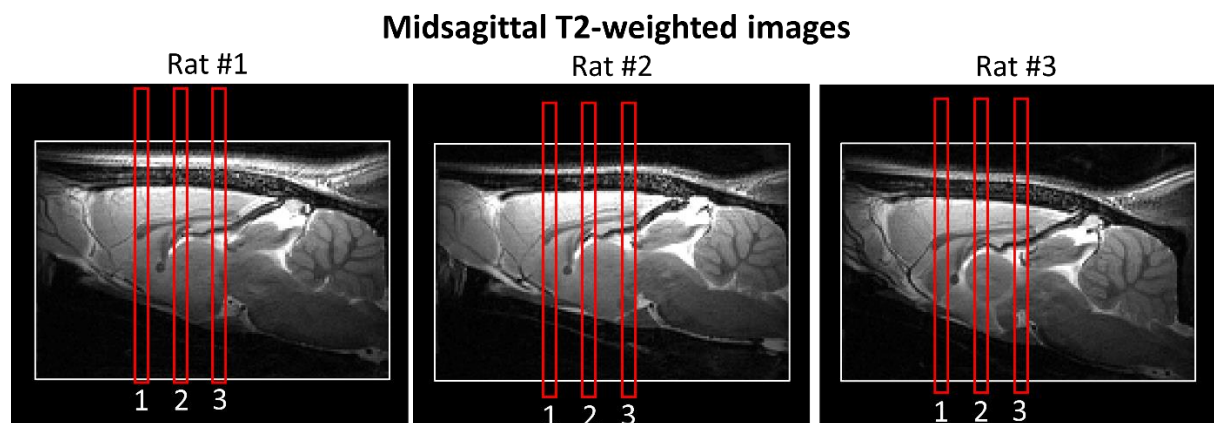


Figure S4 – Midsagittal T2-weighted images of all three animals. These images were used as a reference for placing the 3 coronal slices for diffusion MRI acquisition – positions of the coronal slices are marked in red.

Section F – Long mixing time regime

To empirically check the long mixing time regime, the following two extra DDE set experiments were performed for Rat #1:

- (set #5) acquisitions for $b_1 = b_2 = 1\text{ms}/\mu\text{m}^2$ and parallel DDE directions ($S_5 = \bar{E}_{DDE}(b_1, b_2, 0^\circ)$). For powder-averaging 45 directions of the 8-design repeated 3 times were acquired.
- (set #6) acquisitions for $b_1 = b_2 = 1\text{ms}/\mu\text{m}^2$ and antiparallel DDE directions ($S_6 = \bar{E}_{DDE}(b_1, b_2, 180^\circ)$). For powder-averaging 45 directions of the 8-design repeated 3 times were acquired (note that these directions are inverted for the 2nd encoding).

Other acquisition parameters were equal to the main experiments of these study. Each set was acquired with together with 24 $b_t = 0$ acquisitions for signal decay normalization. Set #5 was also fully repeated 2 times ($S_5^{\#1}$ and $S_5^{\#2}$). Supporting Information Figure S5 shows the powder-averaged signal decays for the two repetitions of set #5 (panels A and B) and for set #6 (panel C). All three experiments show identical signal decays.

The log mixing time regime can be confirmed by checking if the log differences between the powder-averaged signals of set #5 and #6 is near zero (e.g. Jespersen and Buhl, J Magn Reson 2011, Henriques et al., 2020). The maps of the log differences between the two repetitions of data acquisition for set #5 is shown in panel D (for a reference), and the maps of the log differences between signals of set #5 and #6 are shown in panel E. While B0 inhomogeneity artefacts are present in regions outside of the brain for both panels D and E (red arrows), log difference values inside the brain mask are centred in zero. As indicated by the histograms in panel F, ranges of the values for the log difference between signals of set #5 and #6 are identical to the ranges of the values for the log difference between repeated signals of set #5 acquisitions – this shows that the signal fluctuations on the log differences between parallel and antiparallel DDE acquisitions are in the same range than the log differences between repeated noisy signals.

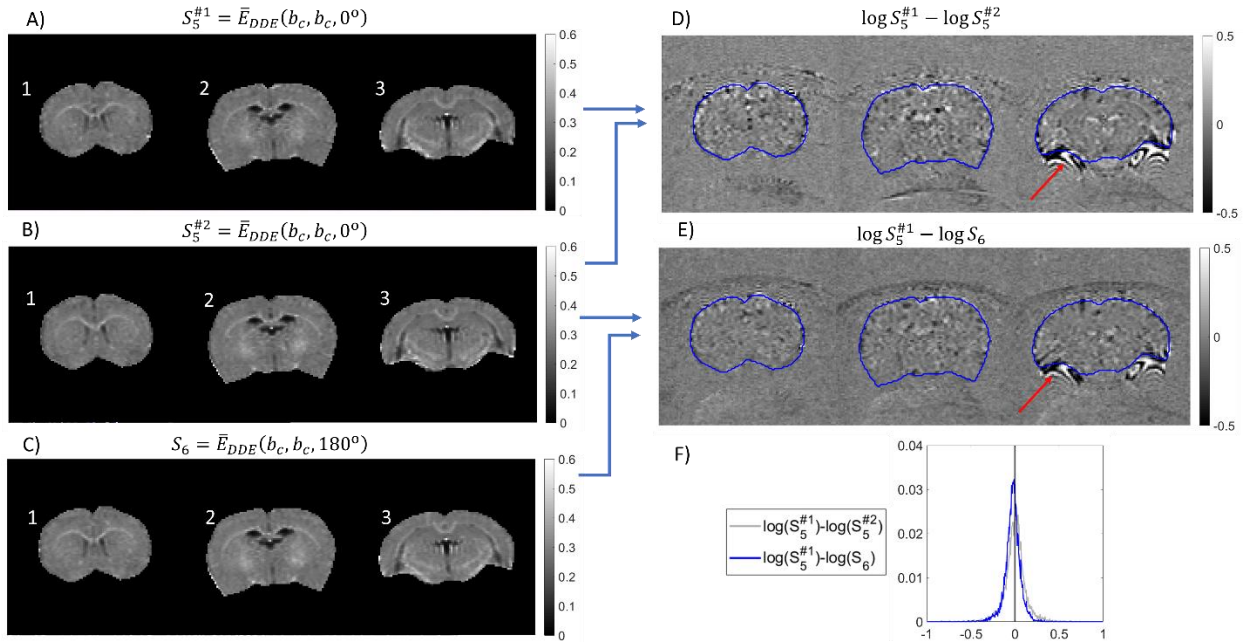


Figure S5 –Powder-averaged data for the extra experiments performed on Rat #1. **A)** Powder-averaged signal decays for DDE parallel acquisitions (repetition #1); **B)** Powder-averaged signal decays for DDE parallel acquisitions (repetition #2); **C)** Powder-averaged signal decays for DDE antiparallel acquisitions. **D)** Map of the log differences values between powder-averaged signals of set #5 repetitions #1 and #2 (brain mask region delineated in blue, and B0 inhomogeneities artifacts are pointed by the red arrow). **E)** Map of the log differences values between powder-averaged signals of set #5 and #6 brain mask region delineated in blue, and B0 inhomogeneities artifacts are pointed by the red arrow). **F)** Histograms of the values inside the brain mask for the log differences values between powder-averaged signals of set #5 repetitions #1 and #2 (grey) and the log differences between powder-averaged signals of set #5 and #6 (blue). Note parameters b_c was set to $1 \text{ ms}/\mu\text{m}^2$ (i.e total b-value = $2 \text{ ms}/\mu\text{m}^2$).

Section G – Data processing (Methods)

Thermal noise of each diffusion-weighted data set and for each cryocoil channel was suppressed using a threshold-based Marchenko-Pastur PCA denoising (92) in which signal components for eigenvalues $\lambda < \sigma^2(1 + \sqrt{N/M})^2$ were removed - σ^2 is noise variance (computed from the repeated $b_t = 0$ acquisitions), N and M are the number of gradient directions pairs and image voxels. The denoised data was subsequently corrected for Gibbs ringing using a sub-voxel shift algorithm (29,93). The processed diffusion-weighted signals for the four channels were then combined using sum-of-squares. Combined data for different gradient direction pairs were then aligned along the different b-values and directions using a sub-pixel registration technique (94).

Section H – MGC kurtosis estimates using sets #2-3

Here we report the results for MGC kurtosis estimates obtained by fitting Eq. 9 to only DDE sets #2, #3, and #4. Under this condition, one can observe that K_{aniso}^{MGC} and K_{aniso}^{CTI} are identical (Supporting Information Figure S6); however, K_{iso}^{MGC} is still a combination of isotropic and microscopic kurtosis effects. Note that these observations can be theoretically derived from Eqs. 6 and 9 as shown below.

MGC K_{aniso} : From Eq. 9, one can note that K_{aniso}^{MGC} can be resolved by:

$$\log \bar{E}_{MGC}(b, 1) - \log \bar{E}_{MGC}\left(b, -\frac{1}{2}\right) = \frac{1}{2} b^2 D^2 K_{aniso}^{MGC} \quad (S3)$$

For $\bar{E}_{MGC}(b, 1) = \bar{E}_{DDE}\left(\frac{b}{2}, \frac{b}{2}, 0^\circ\right)$ and $\bar{E}_{MGC}\left(b, -\frac{1}{2}\right) = \bar{E}_{DDE}\left(\frac{b}{2}, \frac{b}{2}, 90^\circ\right)$, equation S3 is equivalent to Eq. 8 – proving that $K_{aniso}^{MGC} = K_{aniso}^{CTI}$ when MGC kurtosis estimates are obtained from data acquired with identical waveform profiles (i.e. DDE experiments sets #2-3). Note that this would not be the case if data from set #1 is used (i.e., by considering $\bar{E}_{MGC}(b, 1) = \bar{E}_{DDE}(b, 0, 0^\circ)$).

MGC K_{iso} : K_{iso}^{MGC} can be extracted by subtracting $K_{aniso}^{MGC} = K_{aniso}^{CTI}$ from the total apparent kurtosis K_t^{app} of the b-value dependency of $\bar{E}_{MGC}(b, 1)$. Considering that, from the signal decays measured by set #2 and #4, K_t^{app} is equal to $K_{aniso}^{cti} + K_{iso}^{cti} + \frac{\mu K}{2}$ (c.f. Eq. 6), one can show that $K_{iso}^{MGC} = K_{iso}^{cti} + \frac{\mu K}{2}$ - this proves that K_{iso}^{MGC} depends on both sources of isotropic and microscopic kurtosis.

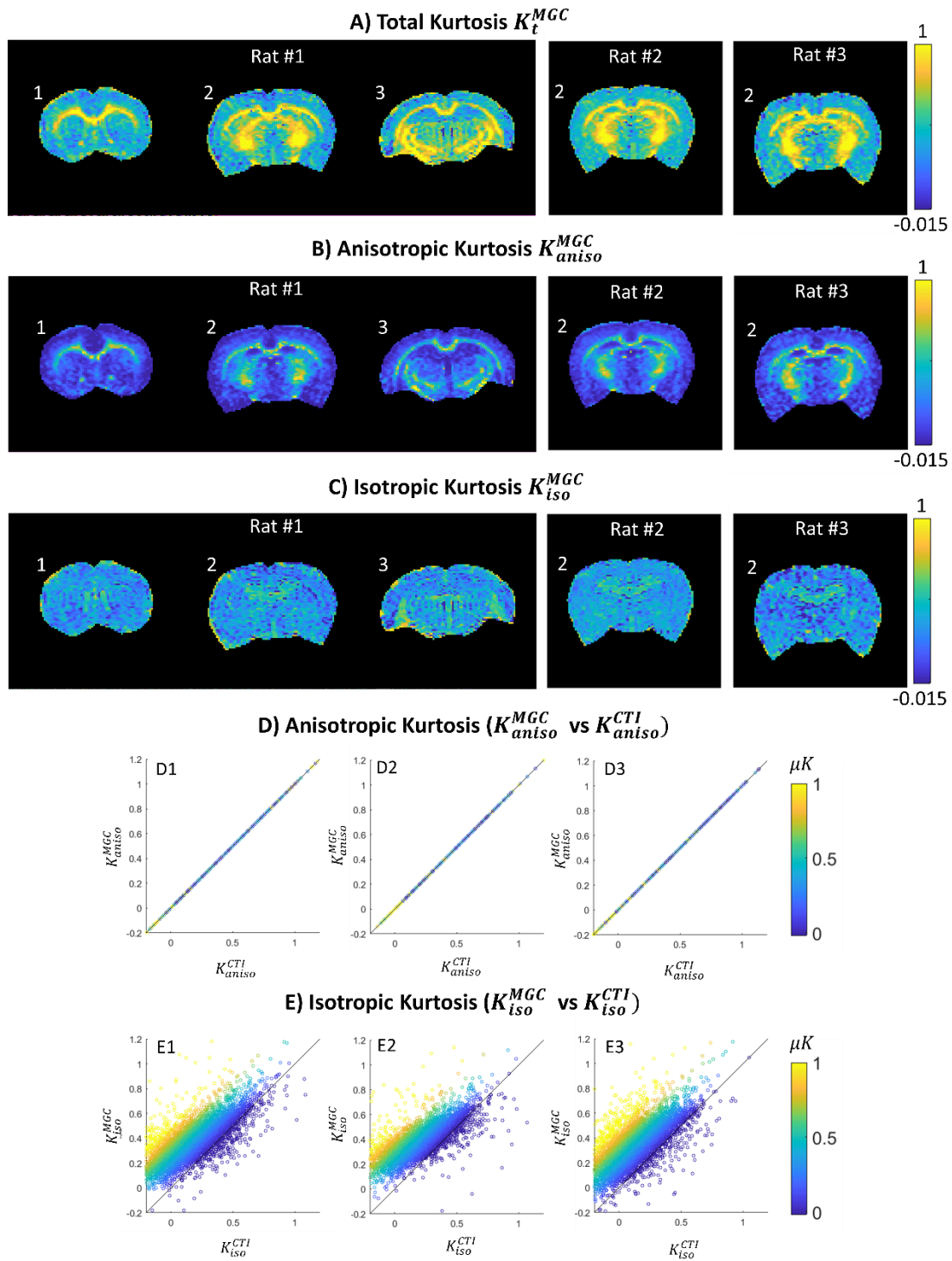


Figure S6 – MGC kurtosis estimates using only data from sets #2, #3, #4 and its comparison to CTI estimates using all data. A) MGC total kurtosis (K_t^{MGC}) maps. B) MGC anisotropic kurtosis K_{aniso}^{MGC} maps. C) MGC isotropic kurtosis K_{iso}^{MGC} maps. D) Scatter plots between MGC anisotropic kurtosis (K_{aniso}^{MGC}) and CTI anisotropic kurtosis (K_{aniso}^{CTI}) estimates; E) Scatter plots between MGC isotropic kurtosis (K_{iso}^{MGC}) and CTI isotropic kurtosis (K_{iso}^{CTI}) estimates.